Scale-dependent brain age with higher-order statistics from structural magnetic resonance imaging

Aurelio Carnero Rosell[a,b], Niels Janssen[c,d,e], Antonella Maselli[f], Ernesto Pereda[d,e,g], Marc Huertas-Company[a,b,h,i], Francisco-Shu Kitaura[a,b,*]

[a] *Instituto de Astrofísica de Canarias (IAC), C/ Vía Láctea, s/n, San Cristóbal de La Laguna, E-38205, Spain*
[b] *Departamento de Astrofísica, Universidad de La Laguna (ULL), E-38206, San Cristóbal de La Laguna, Tenerife, E-38206, Spain*
[c] *Facultad de Psicología, Universidad de La Laguna (ULL), E-38200, San Cristóbal de La Laguna, Tenerife, E-38200, Spain*
[d] *Instituto de Tecnologías Biomédicas (ITB), Universidad de La Laguna (ULL), E-38200, San Cristóbal de La Laguna, Tenerife, E-38200, Spain*
[e] *Instituto Universitario de Neurociencias (IUNE), Universidad de La Laguna (ULL), E-38200, San Cristóbal de La Laguna, Tenerife, E-38200, Spain*
[f] *Institute of Cognitive Sciences and Technologies, National Research Council (CNR), Piazzale Aldo Moro, 7, Rome, 00185, Italy*
[g] *Departamento de Ingeniería Industrial, Universidad de La Laguna (ULL), E-38200, San Cristóbal de La Laguna, Tenerife, E-38200, Spain*
[h] *Observatoire de Paris, LERMA, PSL University, 61 avenue de l'Observatoire, Paris, F-75014, France*
[i] *Université Paris-Cité, 5 Rue Thomas Mann, Paris, 75014, France*

Abstract

Inferring chronological age from magnetic resonance imaging (MRI) brain data has become a valuable tool for the early detection of neurodegenerative diseases. We present a method inspired by cosmological techniques for analyzing galaxy surveys, utilizing higher-order summary statistics with multivariate two- and three-point analyses in 3D Fourier space. This method identifies outliers while offering physiological interpretability, allowing the detection of scales where brain anatomy differs across age groups and providing insights into brain aging processes.

Similarly to the evolution of cosmic structures, the brain structure also

*Corresponding author
Email address: fkitaura@ull.edu.es (Francisco-Shu Kitaura)

evolves naturally but displays contrasting behaviors at different scales. On larger scales, structure loss occurs with age, possibly due to ventricular expansion, while smaller scales show increased structure, likely related to decreased cortical thickness and gray/white matter volume.

Using MRI data from the `OASIS-3` database for the complete sample of 864 sessions (reduced sample: 827 sessions), our method predicts chronological age with a Mean Absolute Error (MAE) of 3.8 years ($\sim$3.6 years) for individuals aged $\sim$40-100 (50-85), while providing information as a function of scale. A neural density posterior estimation shows that the 1-σ uncertainty for each individual varies between $\sim$3 and 7 years, suggesting that, beyond sample variance, complex genetic or lifestyle-related factors may influence brain aging. Applying this method to an independent database, `Cam-CAN`, validates our analysis, yielding a MAE of $\sim$3.4 for the age range from 18 to 88 years. This work demonstrates the utility of interdisciplinary research, bridging cosmological methods and neuroscience.

Keywords: Magnetic Resonance Imaging (MRI), Brain Age, Brain Morphometry, Methods, Statistics
PACS: 87.19.lf, 87.61.Jc, 02.50.Tt, 87.19.lo

---

1. Introduction

The study of brain aging has significant implications for the early detection of neurodegenerative diseases (see, e.g., Bethlehem et al., 2022, and references therein). Understanding how the human brain evolves structurally and functionally over time can provide critical insights into age-related decline and cognitive impairment. Machine learning techniques, particularly those applied to large magnetic resonance imaging (MRI) datasets, have emerged as powerful tools for predicting brain age (Liem et al., 2017; Cole et al., 2017; Fisch et al., 2021; More et al., 2023; Yin et al., 2023; Meng et al., 2024). As discussed in the recent review by Kumari and Sundarrajan (2024), existing models in brain age prediction, such as ensemble methods, support vector regression (SVR), convolutional neural networks (CNN), and recurrent neural networks (RNNs), have been extensively studied and offer specific benefits depending on the task requirements.

Inspired by methods used in cosmology, we propose a novel, transversal higher-order statistical approach to characterize brain aging. In cosmology, the evolution of the cosmic web –complex structures traced by galaxies under

the influence of gravity– can be described as a multidimensional distribution analyzed through higher-order statistics. Similarly, the human brain, which represents the intricate network of connections and structure in the brain, can be studied as a multidimensional distribution, with higher-order statistics revealing structural patterns across different scales. By leveraging two- and three-point statistics in Fourier space, we can capture both large- and small-scale features of the brain anatomy, offering a richer, scale-dependent understanding of how the brain ages over time.

This method does not replace machine learning techniques, but complements them. Our approach introduces a more interpretable framework by identifying the specific scales at which structural changes occur, thereby enhancing the robustness of machine learning predictions.

Moreover, our method provides two key advantages—higher-order statistics (Hindriks et al., 2024) and flexibility across scales—that can be directly compared with traditional neuroscience approaches (Bethlehem et al., 2022; Oschwald et al., 2019; Yang et al., 2024). While conventional methods, such as assessing hippocampal volume or ventricular size, have advanced our understanding of gross structural changes in the aging brain, they often miss subtle changes governed by the nonlinear dynamics of structural relationships across scales. These intricate dynamics can be captured more specifically using multidimensional higher-order statistical Fourier analysis, as demonstrated in this work. By integrating these techniques, we can accurately relate individual brain structure to biological age and potentially gain deeper insight into the physiological processes underlying brain aging, improving early diagnosis of neurodegenerative diseases.

2. Theoretical and mathematical background

Statistical analysis of fields in cosmology often requires understanding their underlying probability distribution functions (PDFs) and their deviations from Gaussianity. These deviations are quantified using moments and cumulants, which describe statistical properties such as variance, skewness, and higher-order interactions. In this section, we introduce the connection between correlation functions, moments, and cumulants, starting from a general non-Gaussian PDF (see, e.g., Bernardeau et al., 2002; Kitaura, 2012, and references therein). For a modern reference to multivariate statistical methods see Pemantle et al. (2024).

2.1. Moments and cumulants of a non-Gaussian PDF

Consider a multivariate probability distribution function $P(\boldsymbol{\nu})$ describing the statistical distribution of a field $I(\mathbf{x})$, where $\mathbf{x}$ is a three-dimensional coordinate (e.g., the voxel center). The variable ν is typically a function of $I(\mathbf{x})$, such as $\nu = I$ or $\nu = I/\langle I\rangle - 1$, the latter being a zero-centered quantity. The n-th order *moments* are defined as:

$$\mu_{i_1\ldots i_n} \equiv \int d\boldsymbol{\nu} P(\boldsymbol{\nu})\nu_{i_1}\ldots\nu_{i_n} = \langle \nu_{i_1}\ldots\nu_{i_n}\rangle, \tag{1}$$

The moment generating function (MGF) is defined as:

$$\mathcal{M}(t_1,\ldots,t_n) \equiv \sum_{q_1\ldots q_n=0}^{\infty} \langle \nu_{i_1}^{q_1}\ldots\nu_{i_n}^{q_n}\rangle \frac{t_1^{q_1}\ldots t_n^{q_n}}{q_1!\ldots q_n!} = \left\langle \exp\left(\sum_{l=1}^{n} t_l\nu_{i_l}\right)\right\rangle , \tag{2}$$

and hence, $\mathcal{M}_{\nu+\eta}(t) = \mathcal{M}_\nu(t)\mathcal{M}_\eta(t)$ (for independent random variables ν and η). Subsequent derivatives of $\mathcal{M}(t_1,\ldots,t_n)$ at the origin $\mathbf{t}=0$ yield the moments:

$$\mu_{i_1,\ldots,i_n} = \left.\frac{\partial^n \mathcal{M}(t_1,\ldots,t_n)}{\partial t_1^{i_1}\cdots\partial t_n^{i_n}}\right|_{\mathbf{t}=0} . \tag{3}$$

Moments capture the overall shape of a distribution but do not distinguish between independent contributions and genuinely correlated structures. To isolate connected correlations, we define cumulants, which are derived from the cumulant generating function (CGF):

$$\mathcal{C}(t_1,\ldots,t_n) \equiv \sum_{q_1\ldots q_n=0}^{\infty} \langle \nu_{i_1}^{q_1}\ldots\nu_{i_n}^{q_n}\rangle_{\mathrm{c}} \frac{t_1^{q_1}\ldots t_n^{q_n}}{q_1!\ldots q_n!} . \tag{4}$$

The cumulants $\kappa_{i_1\ldots i_n} \equiv \langle \nu_{i_1}\ldots\nu_{i_n}\rangle_{\mathrm{c}}$, where the subscript c stands for the connected part, are obtained by taking derivatives of $\mathcal{C}(t_1,\ldots,t_n)$ with respect to the parameters t_i. Specifically, the n-th order cumulant is given by:

$$\kappa_{i_1,\ldots,i_n} = \left.\frac{\partial^n \mathcal{C}(t_1,\ldots,t_n)}{\partial t_1^{i_1}\cdots\partial t_n^{i_n}}\right|_{\mathbf{t}=0} . \tag{5}$$

Since cumulants isolate genuine correlations without mixing information from independent and dependent sources, they must satisfy the additive property for independent random variables: $\kappa_n(\nu+\eta) = \kappa_n(\nu) + \kappa_n(\eta)$.

This property is already exhibited by measures such as the mean and variance for independent variables. Higher-order statistical dependencies should also obey a similar rule if they are to serve as meaningful descriptors of intrinsic structure. Since cumulants are obtained from the derivatives of the CGF, the CGF itself must also satisfy this additivity property: $\mathcal{C}_{\nu+\eta}(t) = \mathcal{C}_\nu(t) + \mathcal{C}_\eta(t)$.

This property suggests that the relationship between the CGF and the MGF follows a logarithmic transformation:

$$\mathcal{C}(t_1, \ldots, t_n) = \log \mathcal{M}(t_1, \ldots, t_n). \tag{6}$$

This transformation ensures that multiplicative relationships between MGFs translate into additive relationships between CGFs.

By combining equations 2, 4 and 6 we obtain:

$$\sum_{q_1 \ldots q_n = 0}^{\infty} \langle \nu_{i_1}^{q_1} \ldots \nu_{i_n}^{q_n} \rangle \frac{t_1^{q_1} \ldots t_n^{q_n}}{q_1! \ldots q_n!} = \exp\left(\sum_{q_1 \ldots q_n = 0}^{\infty} \langle \nu_{i_1}^{q_1} \ldots \nu_{i_n}^{q_n} \rangle_{\mathrm{c}} \frac{t_1^{q_1} \ldots t_n^{q_n}}{q_1! \ldots q_n!} \right). \tag{7}$$

Hence, moments can be expressed as a sum of cumulants, which can be realized by looking at all combinations of connections between points in a diagram, as shown in Figure 1.

The second-order cumulant corresponds to the two-point correlation function:

$$\kappa_2(\mathbf{r}) = \langle \nu(\mathbf{x}) \nu(\mathbf{x} + \mathbf{r}) \rangle_{\mathrm{c}} = \xi(\mathbf{r}). \tag{8}$$

Similarly, the third-order cumulant corresponds to the connected part of the three-point correlation function:

$$\kappa_3(\mathbf{r}_1, \mathbf{r}_2) = \langle \nu(\mathbf{x}) \nu(\mathbf{x} + \mathbf{r}_1) \nu(\mathbf{x} + \mathbf{r}_2) \rangle_{\mathrm{c}} = \zeta(\mathbf{r}_1, \mathbf{r}_2). \tag{9}$$

Higher-order cumulants describe more complex interactions and deviations from Gaussianity. Expanding this function systematically isolates the connected statistical contributions, removing contributions from independent fluctuations.

2.2. Power-spectrum and the two-point correlation function

The power-spectrum $P(\mathbf{k})$ characterizes the two-point statistical properties of a field $\nu(\mathbf{x})$ with $\mathbf{k}$ being the Fourier three-dimensional k-vector. Given its Fourier transform,

$$\hat{\nu}(\mathbf{k}) = \int d^3\mathbf{x}\, \nu(\mathbf{x}) e^{-i\mathbf{k}\cdot\mathbf{x}}, \tag{10}$$

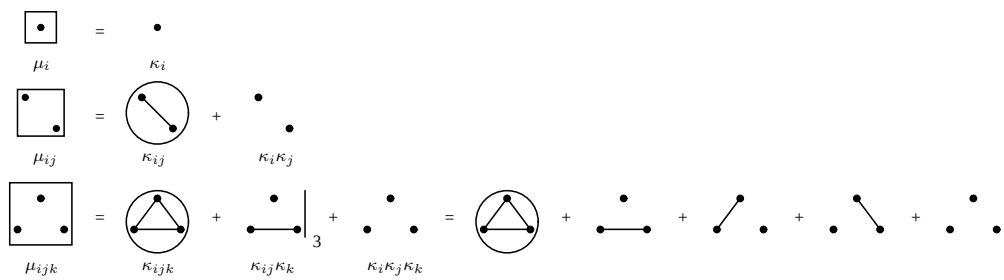

Figure 1: Diagrammatic representation of moments up to third-order correlation statistics (where we choose for simplicity the notation: $i \equiv i_1$, $j \equiv i_2$, $k \equiv i_3$ and each index runs over all voxels). The rectangular boxes denote ensemble averages, corresponding to statistical moments. In the first row we have the mean (in the univariate case: $\langle \nu \rangle = \bar{\nu}$), in the second row we have the relationship for the variance (in the univariate case: $\langle \nu^2 \rangle = \sigma^2 + \bar{\nu}^2$). Dots represent individual data points, with connected dots indicating cumulants (connected moments). The numbers next to certain configurations indicate the count of equivalent terms. Circles highlight the terms that are nonzero, as they lack fully independent components when assuming a centered variable with zero mean. The three equivalent terms of the third-order moment are explicitly shown. A 'cumulant object' is defined as a set of connected points within a moment term, with two cumulant objects considered equivalent if they contain the same number of points.

the power-spectrum is defined as

$$\langle \hat{\nu}(\mathbf{k}) \hat{\nu}^*(\mathbf{k}') \rangle = (2\pi)^3 \delta_{\mathrm{D}}(\mathbf{k} - \mathbf{k}') P(\mathbf{k}), \tag{11}$$

where $\nu^*(\mathbf{k})$ is the conjugate of $\nu(\mathbf{k})$, and δ_{D} the Dirac delta-function. In numerical computations, the power-spectrum is estimated as:

$$P(\mathbf{k}) = \frac{1}{V} \left\langle |\hat{\nu}(\mathbf{k})|^2 \right\rangle, \tag{12}$$

where V is the survey volume, and the averaging is performed over bins in Fourier space.

The power-spectrum is directly related to the two-point correlation function $\xi(\mathbf{r})$, which measures the spatial correlations of a field in real space:

$$\xi(\mathbf{r}) = \langle \nu(\mathbf{x}) \nu(\mathbf{x} + \mathbf{r}) \rangle. \tag{13}$$

The connection between the power-spectrum and the two-point correlation function is given by the Fourier transform pair (according to the so-called Wiener-Khinchin theorem: Wiener, 1930; Khintchine, 1934):

$$\xi(\mathbf{r}) = \int \frac{d^3\mathbf{k}}{(2\pi)^3} P(\mathbf{k}) e^{i\mathbf{k}\cdot\mathbf{r}}, \tag{14}$$

which illustrates how the power-spectrum provides information about the clustering properties of the field in Fourier space.

2.3. Bispectrum and the three-point correlation function

The bispectrum measures the three-point correlations of the Fourier-transformed field and is defined as

$$\langle \hat{\nu}(\mathbf{k}_1)\hat{\nu}(\mathbf{k}_2)\hat{\nu}(\mathbf{k}_3)\rangle = (2\pi)^3 \delta_{\mathrm{D}}(\mathbf{k}_1 + \mathbf{k}_2 + \mathbf{k}_3) B(\mathbf{k}_1, \mathbf{k}_2, \mathbf{k}_3), \tag{15}$$

where the Dirac delta function enforces the triangle closure condition, $\mathbf{k}_1 + \mathbf{k}_2 + \mathbf{k}_3 = 0$.

The bispectrum is related to the three-point correlation function $\zeta(\mathbf{r}_1, \mathbf{r}_2)$, which quantifies the probability of finding triplets of points at separations $\mathbf{r}_1$ and $\mathbf{r}_2$:

$$\zeta(\mathbf{r}_1, \mathbf{r}_2) = \langle \nu(\mathbf{x})\nu(\mathbf{x} + \mathbf{r}_1)\nu(\mathbf{x} + \mathbf{r}_2)\rangle. \tag{16}$$

The Fourier transform relationship between the bispectrum and the three-point correlation function is given by:

$$\zeta(\mathbf{r}_1, \mathbf{r}_2) = \int \frac{d^3\mathbf{k_1}}{(2\pi)^3} \frac{d^3\mathbf{k_2}}{(2\pi)^3} B(\mathbf{k}_1, \mathbf{k}_2, -\mathbf{k}_1 - \mathbf{k}_2) e^{i(\mathbf{k}_1\cdot\mathbf{r}_1 + \mathbf{k}_2\cdot\mathbf{r}_2)}. \tag{17}$$

This highlights how the bispectrum captures non-Gaussian features that are not fully described by the power-spectrum alone.

2.4. Hierarchical model for higher-order correlation functions

Hierarchical models assume that structures exhibit self-similarity, allowing higher-order correlation functions to be constructed from products of the two-point correlation function (Fry and Peebles, 1978; Fry, 1984b,a; Bardeen et al., 1986; Balian and Schaeffer, 1989):

$$\xi_{i_1 \ldots i_n} \equiv \sum_{\alpha} Q_n^{\alpha} \sum_{\mathcal{L}_\alpha} \prod^{n-1} \xi_{ij}\,, \tag{18}$$

such that the full set of points $i_1 \ldots i_n$ is connected by links of ξ_{ij}. These links form a tree structure, where α represents different tree topologies for each order n. The sum over $\mathcal{L}_\alpha$ accounts for all possible labelings of a given tree. The hierarchical coefficients Q_n^{α} encode the remaining degrees of freedom.

For the three-point correlation function, the hierarchical model leads to:

$$\xi_{i_1 i_2 i_3} = Q_3 \sum_{\text{permutations}} \xi_{i_1 i_2} \xi_{i_1 i_3}, \tag{19}$$

where Q_3 is the single hierarchical coefficient at third order.

In Fourier space, the normalized ($Q_3 = 1$) hierarchical bispectrum is defined as:

$$B_{\mathrm{h}}(\mathbf{k}_1, \mathbf{k}_2, \mathbf{k}_3) = P(k_1)P(k_2) + P(k_2)P(k_3) + P(k_3)P(k_1), \tag{20}$$

which leads to the definition of the reduced bispectrum, highlighting non-Gaussian deviations:

$$Q(\mathbf{k}_1, \mathbf{k}_2, \mathbf{k}_3) = \frac{B(\mathbf{k}_1, \mathbf{k}_2, \mathbf{k}_3)}{B_{\mathrm{h}}(\mathbf{k}_1, \mathbf{k}_2, \mathbf{k}_3)}. \tag{21}$$

This formulation accounts for expected Gaussian-like hierarchical structures and isolates deviations from Gaussianity.

3. Method

Within the framework of information theory, the set of voxels in a three-dimensional image can be interpreted as a probability distribution function, shaped by an underlying physical and observational process.

An image, such as an MRI image, is always defined over a finite, positive range. The intensity distribution from such images, modeled by a compactly supported PDF, is constrained to a bounded domain. Despite this finite support, the complexity of the underlying intensity distribution can be arbitrarily high, reflecting intricate anatomical or (physio-)pathological structures. However, the advantage of distributions with finite support is that their moment sequences are often better behaved, and the information encoded in these moments is more constrained. In many cases, the moments uniquely determine the distribution—a property known as moment determinacy—without requiring additional regularisation or assumptions that are necessary for distributions with infinite or unbounded support (Stoyanov et al., 2020). This makes finite-support distributions particularly suitable for moment-based analysis (Hausdorff, 1921a,b; Shohat and Tamarkin, 1943).

Since we are dealing with three-dimensional data we have to consider correlation functions of multivariate PDFs, for which each voxel of the MRI image represents one statistical dimension.

Analogously to the two-point correlation function of galaxies, which is a function of distance and describes the excess probability of finding two galaxies separated by this distance (Peebles, 1980), we consider the correlation of voxels based on their intensities. This is computed in Fourier-space, yielding the so-called power-spectrum (see section 2 and Vazza and Feletti, 2020, for a power-spectrum study of dead brain structures). Distributions with identical two-point statistics can have very different three-dimensional patterns (Kitaura et al., 2015). Thus, we need to resort to higher-order statistics.

The three-point correlation function has a long history in cosmological astronomy. It was already computed in configuration space in the 70s from the three-dimensional galaxy distribution (Groth and Peebles, 1977). Later, it was extended to Fourier-space, the so-called bispectrum (Baumgart and Fry, 1991). The three-point statistics can be exploited to probe models of structure formation (Frieman and Gaztanaga, 1994) and the bias from dark matter tracers (Matarrese et al., 1997). It has the powerful property of capturing deviations from a Gaussian distribution, and can thus be extremely sensitive to the complex multidimensional patterns beyond the two-point statistics. Controlling both two- and three-point statistics of complex structures provides a powerful approach for accurate modeling. For example, the distribution of galaxies and their dynamics are successfully reproduced by constraining model parameters using two- and three-point statistics, as demonstrated in previous work where the same software used here was applied to galaxy survey data (Kitaura et al., 2016).

In this study, as part of the `Cosmic Brain` project, we rely on the combined power-spectrum and bispectrum analysis (see section 2, Figure 2 and corresponding explanation in Appendix B). In Fourier-space, signals are decomposed into different frequency components, to different spatial scales. This allows for a more detailed and clear understanding of how structural changes manifest at different scales. For brain anatomy, this is crucial because aging or neurodegenerative processes impact large-scale (global) and small-scale (local) brain structures differently, as we will show below. A detailed description of the method presented in this work can be found in Appendix D.

4. Results

Our sample consists of a complete sample (CS) of 864 MRI sessions and a reduced sample (RS) of 827 MRI sessions from "healthy" subjects in the

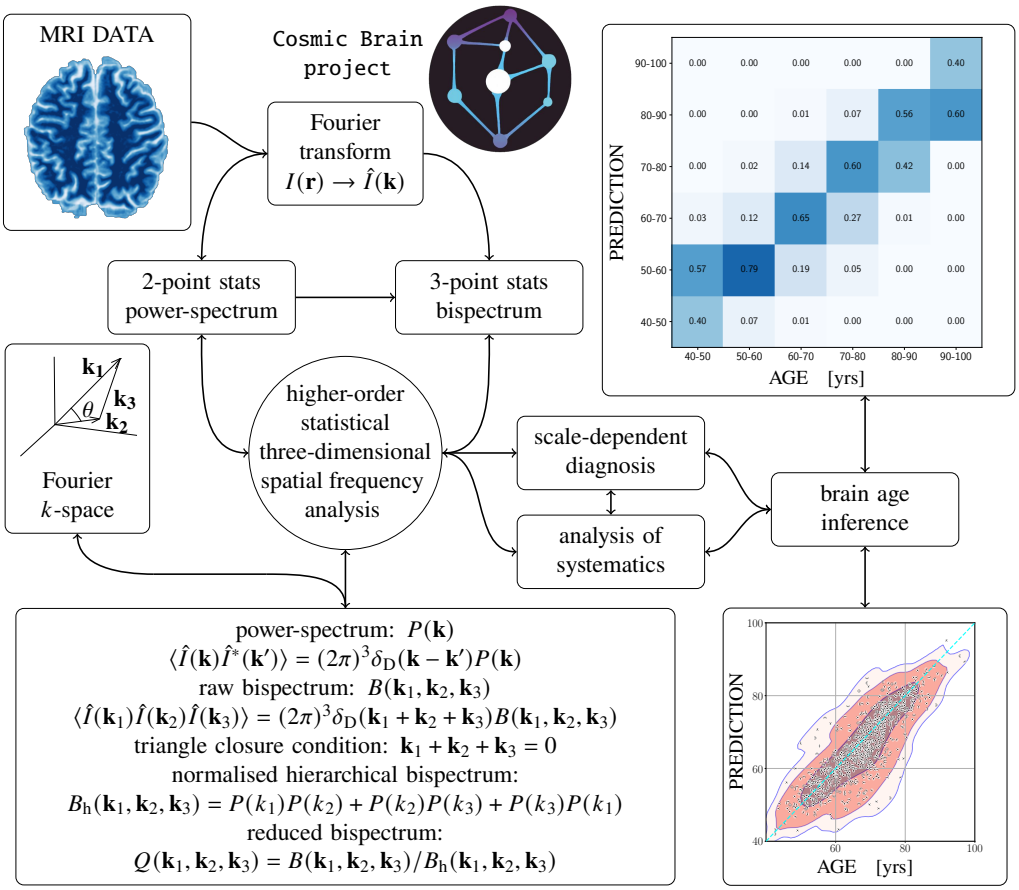

Figure 2: Summary of the higher-order statistical three-dimensional spatial frequency analysis method for brain age inference (as part of the `Cosmic Brain project`), showing the process from the input MRI data (top-left) to the outcome (right): confusion matrix (top-right) and regression between the predicted brain age and the actual chronological age (bottom-right). The MRI data can be represented as an intensity array $I(\mathbf{r})$ in a cubical mesh with voxel coordinates $\mathbf{r} = \{r_x, r_y, r_z\}$. The Fourier transform of $I(\mathbf{r})$ is represented by $\hat{I}(\mathbf{k})$ as a function of the k-vector. The power-spectrum $P(\mathbf{k})$ represents a measure of the two-point clustering statistical (squared) amplitude as a function of spatial frequency distance, while the bispectrum $B(\mathbf{k}_1, \mathbf{k}_2, \mathbf{k}_3)$ represents the analogous quantity for the three-point statistics, as a function of triangle configurations. $\hat{I}^*(\mathbf{k})$ is the conjugate of $\hat{I}(\mathbf{k})$, and $\delta_{\rm D}$ is the Dirac delta function.

OASIS-3 database. Further details on sample preparation and selection are provided in Appendix A.

The CS sample includes subjects aged 42 to 98 years, though the distribution is notably sparse below 50 and above 85. Consequently, while we use the entire age range in the analysis, we exclude the ranges below 50 and above 85 from the final validation process with the RS sample.

We have focused on the age range (both CS and RS samples), during which lifestyle factors begin to significantly influence brain health, and the likelihood of neurodegenerative diseases increases.

We calculate the power-spectra and bispectra for 975 triangular configurations from the CS sample, thus measuring the two- and three-point statistics in Fourier-space. In particular, we run over triangle configurations given the length of two sides as a function of the subtended angle, θ. Considering the size of human brains and the resolution of the MRI data we consider the spatial frequency range from $k = 0.1$ mm^{-1} to $k = 2$ mm^{-1} in Fourier-space, equivalent to $r \approx 3$ mm and $r \approx 63$ mm in configuration space.

We include two types of bispectra in the analysis: raw and reduced ones (see section 2). Since the reduced bispectrum is computed as the raw bispectrum divided by the hierarchical bispectrum model, which is constructed from the sum of permutations of power-spectrum products, a combined analysis of raw and reduced bispectra effectively integrates information from both two-point and three-point statistics.

4.1. Brain age dependence on the higher-order statistics

We find that the power-spectrum shows a nearly linear, moderate correlation of amplitude with age (see upper-left panel in Figure 3), suggesting limited potential as a standalone biomarker for brain age prediction. In contrast, both the raw and reduced bispectra exhibit a clear, complex, and strong correlation with brain aging (see the remaining panels in the same figure). The ordering of the curves by age groups is visually apparent in the fanned-out bispectrum curves, highlighting the potential of this technique as a tool for diagnosing neurodegenerative diseases.

In addition, we can express the variation of the bispectrum with respect to a hierarchical model through the reduced bispectrum to enhance the signal-to-noise ratios at different scales. We find that reduced bispectra are more sensitive on larger scales, while raw bispectra are more sensitive to small scales. This behaviour is quantified through Kendall's rank correlation coefficient τ applied to the CS sample and shown in Appendix C (Kendall,

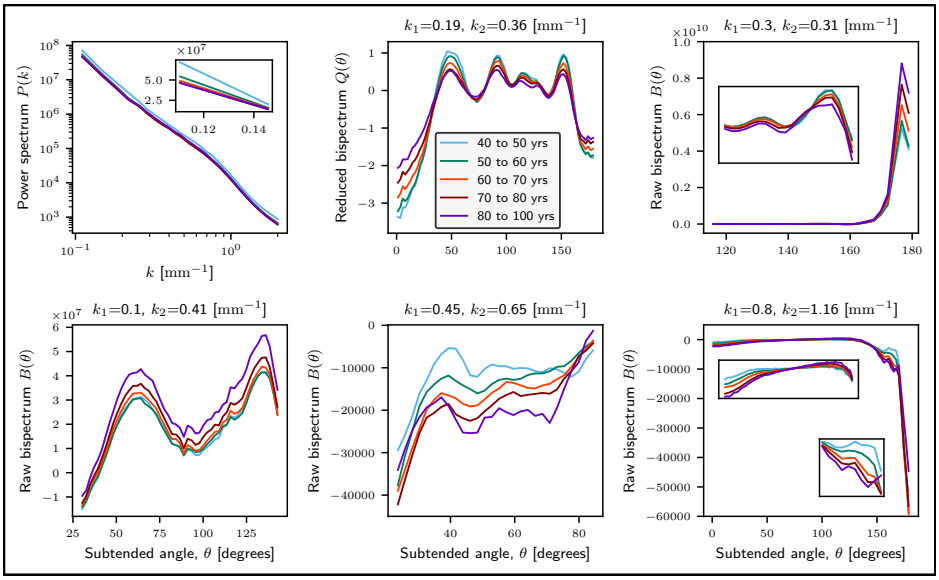

Figure 3: Median power-spectra (top-right panel) and bispectra (bottom-left, middle and right panels) per age group for the individual configurations that enter the biomarker definition from the CS sample. Here we consider the raw and reduced bispectra for fix $|\mathbf{k}_1|$ and $|\mathbf{k}_2|$ as a function of the subtended angle θ between both k-vectors: $B(\theta|k_1, k_2)$ and $Q(\theta|k_1, k_2)$

1938, 1945), which is better suited than Pearson's correlation, as it does not assume a linear relationship, but evaluates how well the ranks of one variable correspond to the ranks of another variable.

Since the complexity in the three-dimensional structure can be characterised by the deviation from a flat bispectrum, we propose to use the variance for each bispectrum configuration as a measure of that deviation. The average bispectrum variance helps identify outliers within age groups, which may result from MRI measurement artifacts, early signs of dementia, or general anatomical anomalies—referred to as systematics in the context of our study. For details on the selection criteria, see Appendix A.2. In future studies, with more data available, we plan to investigate these outliers in greater depth to determine whether they are due to systematics or represent healthy individuals with unique brain evolution linked to particular lifestyle factors.

4.2. Statistical analysis

First we evaluate the pool of 975 triangle configurations for the complete sample CS. To estimate the performance of each configuration as a potential

biomarker, we employed a Random Forest classifier (see Breiman, 2001) using a leave-one-out cross-validation (LOO-CV) technique (Hastie et al., 2001), ensuring that each subject's estimate was independent of the training sample (see Appendix D for further explanation on the algorithm).

To assess the classification performance, we calculate the MAE and the geometric mean score (G-Mean, defined as the square root of the product of class-wise sensitivity), both as overall averages and as functions of age (see Appendix C for details on the metric computations).

A practical biomarker should not rely on ∼thousands of computationally expensive Fast Fourier Transform (FFT) calculations. Additionally, many of these configurations likely contain redundant information or exhibit weaker correlations with age compared to others. Therefore, it is essential to reduce the number of informative configurations to a small subset that can be computed within a few minutes per patient for potential clinical applications, without compromising diagnostic accuracy.

To this end, we initially identify the top four bispectrum configurations based on average metrics. We then select the configuration with the highest G-Mean, the one with the smallest G-Mean variation across age, and finally, the two configurations that most effectively classify subjects in the youngest and oldest age groups. This approach helps to minimize biases towards the boundaries of the sample.

After selecting the five top singular configurations, we generated all possible combinations and we chose the combination that optimized the MAE metric, based on a neural network we designed for age regression (see Appendix D for a further explanation on the algorithm).

We also tested the inclusion of the power-spectrum in combination with the bispectra and found no improvement. Hence, the two-point statistics is only taken into account through the hierarchical bispectrum in the reduced bispectrum configuration.

In Appendix C, we compare the performance metrics of different configurations, demonstrating how combining singular configurations into a single vector improves predictive accuracy. We present three metrics as a function of age: G-Mean, the percentage of outliers in the predictions (defined as cases where the predicted age deviates by more than 7 years from the chronological age) and the MAE, for both singular configurations and the final biomarker. The proposed biomarker incorporates the following five bispectrum configurations: the three with the best global average metrics, the one with the smallest variation, and the one that best predicts the oldest age group.

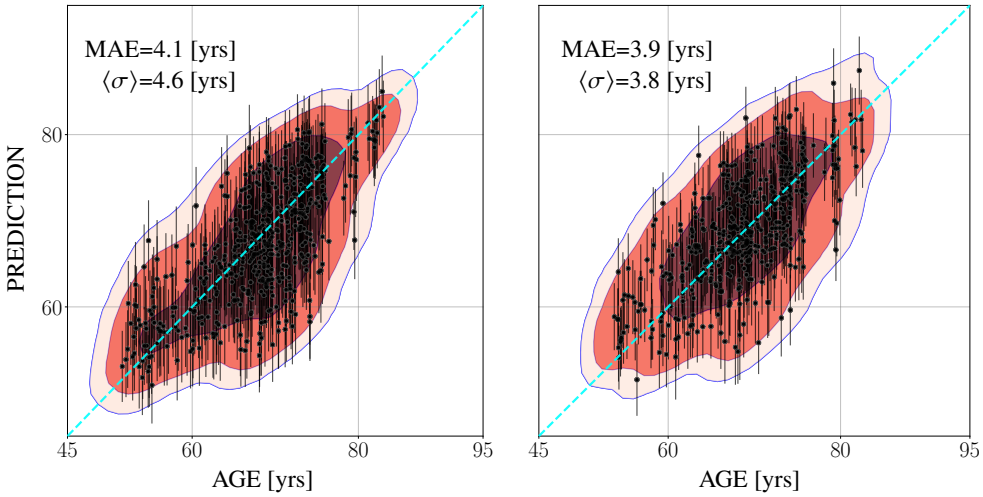

Figure 4: Regression based on the CS (left panel) and the RS sample (right panel), using a neural density posterior estimator indicating the MAE and the average standard deviation per subject.

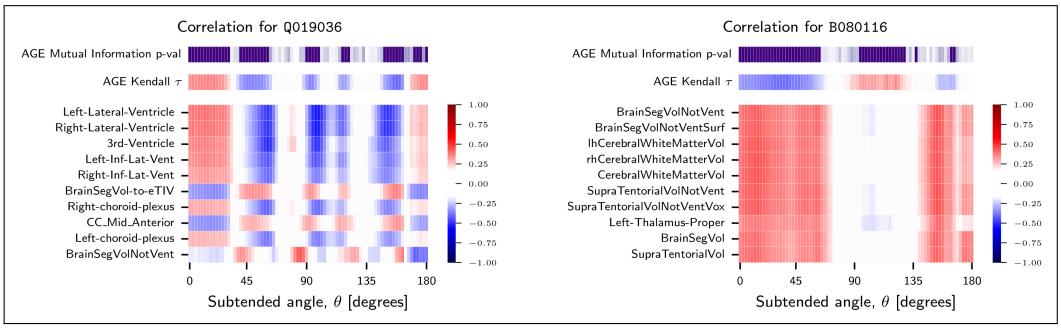

Figure 5: At the top of both panels, p-values from mutual information analysis for bispectra across subtended angles with age (purple color indicates strong dependence: $p < 0.001$). Below that, Kendall's rank correlation to the bispectra for two configurations are shown: with age (top) and with the ten most significant anatomical variables from `Freesurfer`. In particular, at the scales of `Q019036`, the effect of ventricle volumes is highlighted, while at smaller scales in `B080116`, the bispectrum is more sensitive to white matter content. Red indicates positive correlation, while blue represents negative correlation or anti-correlation.

First we apply the analysis to the CS sample of 864 sessions. The bottom-right panel of Figure 2 presents the scatter plot comparing chronological age with the predicted age, as obtained using the age-regression neural network developed in this study. In a categorical approach, using an incompleteness weight correction in the Random Forest classification (class-weight balance sub-sample), the top-right panel of the same figure shows the confusion matrix for age groups in ten-year intervals. The overall MAE for the CS sample is 3.8 years.

The limited sample size at the youngest and oldest age ranges likely contributes to poorer performance in these groups. When the analysis is restricted to the 50 to 85 age range using the RS sample, without applying an incompleteness weight correction, the average MAE improves to 3.6 years.

Comparable performance is obtained using neural density estimators to approximate the amortized posterior distribution of the age given the higher-order statistics (see Appendix D.1). As shown in Figure 4, the results are in line with those obtained from the age-regressor neural network, although the neural density estimators exhibit slightly higher MAE values. This discrepancy may be attributed to the small sample size and the non-uniform implicit prior distribution, which could affect the accuracy of the estimators. For the CS sample we can obtain in some realizations a close MAE to that from the age-regressor (4.1 years), but for the RS sample the best MAE we have found is 3.9 years, which differs more from the age-regressor result. However, the variability in the answer depending on the randomly chosen training dataset can typically yield MAE values as large as $\sim$4.3 years or in some cases even higher. The neural density estimators reveal that uncertainty, as measured by the 1-σ value, varies significantly between individuals. In the RS sample, for instance, the uncertainty for individuals aged 75 to 80 years ranges from as low as 3.3 years to nearly 7 years, likely due to gaps in the data for this age group. In contrast, the CS sample shows the largest deviation, exceeding 2 years, in the 65 to 70 age group, despite having the most data available. This suggests that even with abundant data, substantial uncertainty can persist, possibly due to underlying complexities specific to that age group. This variation highlights the influence of peculiar features in the higher-order statistics, likely linked to unique lifestyle factors (if imaging quality issues can be ruled out), on the model's predictive confidence. In future work, we aim to explore the calibration and robustness of the estimated posteriors in greater detail with larger datasets, to obtain more precise uncertainty quantification for each patient (see Appendix D for further details).

The irregular, noisy patterns observed in the raw bispectrum configurations, suggest that there is potential for improvement with the availability of more data. It is important to note, however, that lifestyle factors increasingly influence biological brain age as individuals grow older. Nonetheless, we plan to explore the completeness of the information in the summary statistics by extending this study to smaller-scale bispectrum configurations and the trispectrum (four-point statistics), while also conducting brute-force analyses on using the full cubical MRI data volumes (see, e.g., methods such as García-Farieta et al., 2024).

To further validate our method, we applied the same prescription directly to the `Cam-CAN CC700` dataset (Taylor et al., 2017; Shafto et al., 2014). Even though the characteristics of this dataset is significantly different from `OASIS-3` we obtain qualitatively similar results (MAE for the age range: 18-88: ~ 3.4). In particular, we find that some of bispectrum configurations obtained from `OASIS-3` are still valid in `Cam-CAN`, even though they sample different age ranges with different densities and populations (see Appendix E for details).

5. Neuroanatomical and physiological interpretation

We present a correlation study between the bispectrum configurations and the neuroanatomical variables of the brain. In particular, we focus on Kendall's rank-correlation analysis. Nonetheless, we have performed also a p-value mutual information calculation which confirms Kendall's analysis results (see Figure 5).

5.1. Scale-dependent analysis

Since the bispectrum configuration is determined by two wavenumbers, k_1 and k_2, which define the sides of a triangle in Fourier space, it captures interactions across different spatial scales. Considering that the Fourier wavenumbers are inversely proportional to the scale:

- **Small k_1, k_2 values**: Correspond to large-scale structures, capturing global brain morphology changes, such as cortical shrinkage and ventricular expansion.
- **Large k_1, k_2 values**: Reflect fine-scale structures, highlighting local variations in cortical thickness, white matter integrity, and microstructural degradation.

- **Intermediate configurations**: Represent mixed-scale interactions, where structural correlations exist between global and local features.

- **Bispectrum angles**: The angular relationships between k_1 and k_2 further refine the interpretation, with small angles representing interactions between similar-scale structures and intermediate to large angles reflecting multi-scale dependencies. This is confirmed by the similar correlation values in Figure 5 comparing small and large angles.

The angle θ between k_1 and k_2 defines how different scales interact within a bispectrum triangle:

$$\cos(\theta) = \frac{k_1^2 + k_2^2 - k_3^2}{2k_1k_2}, \tag{22}$$

according to the law of cosines, where k_3 is the third side of the triangle, constrained by the triangle inequality. The angular dependence plays a crucial role in the interpretation of bispectrum correlations:

- **Small angles ($\theta < 30°$)**: These correspond to nearly collinear wavevectors ($k_1 \approx k_2$), meaning the bispectrum predominantly captures self-similar interactions at the same scale.

- **Intermediate angles ($30° < \theta < 170°$)**: These angles represent configurations where k_1 and k_2 are significantly different, leading to cross-scale interactions that mix structures of smaller and larger scales.

- **Very large angles ($\theta > 170°$)**: These correspond to nearly anti-parallel wavevectors, meaning k_1 and k_2 point in opposite directions but maintain similar magnitudes. This configuration behaves similarly to small angles because it still emphasizes self-similar interactions, but mirrored across larger spatial extents. The structural features captured here resemble those at small angles.

This symmetry in behavior between small and very large angles arises from the geometry of Fourier interactions: when wavevectors are nearly collinear or anti-parallel, the dominant structural patterns remain confined to closer-scale interactions, whereas intermediate angles introduce scale-mixing effects that modify the correlation patterns. In particular, the bispectrum in the squeezed limit, i.e., for $k_3 \ll k_1, k_2$, can be expressed in a more compact

form and is widely studied in cosmology (see, e.g., Creminelli et al., 2011; Pajer et al., 2013).

It is important to note that, in general, we are considering configurations where k_1 and k_2 are significantly different, except in the case of `B030031`. When $k_1 \simeq k_2$, the bispectrum in the squeezed limit admits a simpler expression that depends solely on a function of the power-spectrum.

Additionally, we distinguish between reduced and raw bispectra. Thus, by analyzing the correlation between bispectrum configurations and anatomical features, we are studying how different spatial interactions in the brain relate to specific neuroanatomical structures.

5.2. Interpreting the brain structures in relation to bispectrum features

The brain regions analyzed can be broadly classified into ventricular structures, cortical structures, and volume-based measures, each having distinct physiological significance:

5.2.1. (a) Ventricular System (CSF Spaces)

- **Left-Lateral Ventricle, Right-Lateral Ventricle, 3rd Ventricle, Left-Inf-Lat-Ventricle, Right-Inf-Lat-Ventricle**
  - These structures contain cerebrospinal fluid (CSF) and expand with brain atrophy (e.g., in neurodegenerative diseases).
  - Strong bispectrum correlations with these ventricles may indicate that specific scales of non-Gaussianity are linked to ventricular enlargement, which is a biomarker for neurodegeneration (e.g., Alzheimer's, hydrocephalus).
  - For small angles ($k_1 = 0.19$, $k_2 = 0.36$) in the reduced bispectrum, Kendall's rank correlation is close to 1 for the Left-Lateral Ventricle, Right-Lateral Ventricle, 3rd Ventricle, and Left-Inf-Lat-Ventricle, showing a strong positive relationship. Hence, ventricular structures are well captured by large scale (low k-mode) bispectrum configurations.
  - The correlation is slightly lower but follows the same trend for the Right-Inf-Lat-Ventricle, right-/left-choroid-plexus.
  - For intermediate angles, the correlation reverses, approaching -1 for these ventricular structures. This strong anticorrelation suggests that bispectrum features at these scales are sensitive to ventricular expansion but in an opposite manner: larger ventricles

correspond to lower bispectrum amplitudes in these configurations. This could imply a shift in the dominant spatial patterns of non-Gaussianity, potentially reflecting anatomical remodeling or differential sensitivity to tissue-CSF contrast at intermediate scales.

5.2.2. (b) Brain Volume and Cortical Measures

- **BrainSegVol-to-ETIV (Brain Segmentation Volume to Estimated Total Intracranial Volume)**
  - This ratio is a normalized brain volume measure, adjusting for head size.
  - Correlations with bispectrum suggest that certain spatial scales of non-Gaussianity are predictive of brain volume loss.
  - For small angles in the reduced bispectrum ($k_1 = 0.19$, $k_2 = 0.36$), Kendall's rank correlation is close to -1, suggesting that increased bispectrum strength is associated with a reduction in brain volume. This implies that large-scale bispectrum features are primarily capturing structural atrophy patterns, where a decrease in brain volume corresponds to an amplification of non-Gaussianities at these scales.
  - At intermediate angles, the correlation flips to approximately 1, indicating that bispectrum features at these scales track brain volume in an opposite manner. This suggests that at intermediate Fourier modes, non-Gaussian structure may be reflecting localized cortical thinning, tissue heterogeneity, or compensatory spatial reorganization rather than global atrophy, leading to an inverse dependence on bispectrum strength compared to larger scales.

5.2.3. (c) White Matter and Supratentorial Volumes

- For the raw bispectrum configuration with $k_1 = 0.80$ and $k_2 = 1.16$:
  - For both small and large angles, Kendall's rank correlation is very close to 1 for:
    - **BrainSegVolNotVent**: Measures total brain volume excluding ventricles.
    - **BrainSegVolNotVentSurf**: Similar to BrainSegVolNotVent but calculated using surface-based methods.

    - **Left and Right Cerebral White Matter Volumes (lh/rhCerebralWhiteMatterVol)**: Quantifies the volume of white matter in each cerebral hemisphere.
    - **CerebralWhiteMatterVol**: Total cerebral white matter volume, combining left and right hemispheres.
    - **SupratentorialVolNotVent/Vox**: Measures the volume of the brain above the tentorium, excluding ventricles, with a voxel-based estimation.
    - **Left Thalamus Proper**: Represents the volume of the left thalamus, a critical relay center in the brain.
    - **BrainSegVol**: Total segmented brain volume, including both gray and white matter.
    - **SupratentorialVol**: Total supratentorial volume, including ventricles.
  - This strong positive correlation suggests that raw bispectrum configurations at this scale are highly sensitive to global and regional white matter integrity and supratentorial structures.
  - Intermediate angles for this configuration yield near-zero correlation across all variables. This suggests that these spatial interactions do not predominantly capture local, nor global morphological features, nor structural dependencies at mixed scales, unlike small and large angles, which emphasize self-similar structures.

Strong deviations from Gaussianity in the ventricular system (high correlation in the reduced bispectrum) suggest that ventricular expansion is associated with non-trivial morphological alterations beyond simple volumetric enlargement, possibly reflecting asymmetries, shape distortions, or interactions with surrounding structures. In contrast, a strong negative correlation between the reduced bispectrum and brain volume measures (e.g., BrainSegVol, SupratentorialVol) indicates that as brain atrophy progresses, the brain's spatial organization deviates from a hierarchical Gaussian framework, likely due to selective tissue loss patterns.

5.3. Conclusion

By cross-checking the correlations between bispectra, anatomical variables, and age, we confirm key features related to brain aging, such as ventricle volume expansion, white matter reduction, and choroid plexus involvement in brain aging.

These findings align with prior studies (Bethlehem et al., 2022; Dani et al., 2021; Choi et al., 2022; Danielsen et al., 2020) and reinforce that the bispectrum captures meaningful higher-order structural variations.

To further support this analysis we plan to conduct a more in-depth study based on simulated data (see, e.g., Wen et al., 2022; Bhattarai et al., 2024; Yang et al., 2022).

6. Discussion

The findings in this work demonstrate the utility of higher-order summary statistics in understanding the relationship between brain aging and structural changes in brain anatomy and physiology. By employing two- and three-point statistics in Fourier-space, we developed a methodology capable of predicting chronological brain age while offering interpretable insights into the underlying physiological processes. This approach provides a novel avenue for uncovering age-related changes in brain structure. Furthermore, this method has the potential to enhance the accuracy of machine learning models by providing highly informative measures and effectively cleaning the data samples by detecting and removing outliers caused by measurement issues.

6.1. Connection to cosmology

The foundation of this work lies in an analogy between the statistical distribution of the brain and the cosmic web structure of galaxies evolving over time. Unlike cosmic surveys, where finite volume and observational limitations necessitate correction, brain volume inherently correlates with age (Fujita et al., 2023). Therefore, while skull standardization was applied to standardize volume measurements (see Appendix A), no additional corrections for the brain mask were implemented. Future work may explore more refined masking strategies.

A central insight from our analysis is the behavior of the MRI intensity power-spectrum and bispectrum across different scales and ages, drawing parallels to the cosmic density field studied in cosmology. The upper left panel of Figure 3 shows the power-spectrum evolution across different age groups. Similar to the growth of large-scale cosmological structures, we observe a near-linear evolution of large brain structures with decreasing age.

To assess nonlinear brain evolution, we analyzed the three-point statistics. The upper central panel of Figure 3 displays the nonlinear evolution of brain

structures through the reduced bispectrum for large-scale triangle configurations. Here, younger individuals exhibit greater variability in large-scale structures than older individuals, suggesting greater structural complexity in early adulthood. This aligns with previous findings on the progressive simplification of brain structure with age, likely due to ventricular expansion. The analogy to cosmic evolution is notable: just as the universe appears more homogeneous at earlier times (Springel et al., 2005), brain structure appears to lose complexity with aging. This relationship between large-scale structural loss and brain aging supports previous studies (Yang et al., 2024; Bethlehem et al., 2022; Oschwald et al., 2019), highlighting the potential of the bispectrum as a diagnostic tool for neurodegenerative diseases.

Conversely, the raw bispectrum (bottom-right panel of Figure 3) reveals increasing structural complexity at smaller scales in older individuals. This is likely linked to the reduction in gray and white matter volume with age. In analogy to galaxy formation, where mergers occur in regions of high dark matter density, the reduction in brain matter may induce a "folding" or compactification of brain structures. This mirrors processes observed in cosmological phase-space evolution. As gray and white matter decrease, the remaining brain structures may reorganize into a more intricate spatial configuration, compensating for volume loss.

6.2. Bispectrum, Kendall's rank correlation and mutual information analysis

Our bispectrum analysis, combined with Kendall's rank correlation, and mutual information calculations, provides further insights into how structural changes in the brain manifest across different scales and configurations. We identified key differences in correlations based on bispectrum angles and wavenumber configurations.

For **Small angles ($\theta < 30°$) and very large angles ($\theta > 170°$)**:

- **Large-scale interactions: reduced bispectrum configuration ($k_1 = 0.19, k_2 = 0.36$)**:
  - Strong positive correlations with ventricular volumes (left and right lateral ventricles, third ventricle, inferior lateral ventricles), suggesting that large-scale morphological changes such as ventricular expansion are major drivers of non-Gaussian features in brain aging.

  - Negative correlations with total brain volume measures (e.g., BrainSegVol-to-ETIV, corpus callosum mid-anterior), reinforcing the interpretation that structural degradation and atrophy reduce overall brain complexity.

- **Small-scale interactions: raw bispectrum configuration** ($k_1 = 0.80, k_2 = 1.16$):
  - High positive correlation with white matter and supratentorial volume measures, implying that fine-scale cortical and white matter integrity strongly contribute to bispectrum variability at these scales.
  - As age increases, the raw bispectrum captures an increase in structural complexity at small scales, possibly due to cortical folding compensation mechanisms as white and gray matter decline.

These findings indicate that the bispectrum serves as a powerful tool for detecting age-related structural transformations, distinguishing between large-scale atrophy (ventricular expansion) and fine-scale changes in cortical and white matter structure. The observed scale-dependent patterns reinforce the idea that the brain undergoes a systematic transition from a more complex, interconnected state in early adulthood to a simplified, functionally reorganized state in aging.

6.3. Gender differences

Internal tests indicated that analyzing males and females separately did not significantly enhance classification sensitivity. Thus, we proceeded with a gender-agnostic approach. This is likely influenced by sample size limitations, as there is evidence that aging processes differ by biological sex (Liem et al., 2017). Future studies with larger datasets could explore potential sex-based differences in more depth.

6.4. Interdisciplinary approach and future directions

The interdisciplinary framework presented here bridges cosmology and neuroscience, providing a novel perspective on brain aging. By drawing parallels to the cosmic web, where large-scale structures evolve through gravitational interactions, we gain deeper insights into how the brain undergoes structural reorganization over time. The combination of power-spectrum and

bispectrum methods enables us to detect features that traditional techniques may overlook.

A key advantage of this method is its versatility. It can be applied beyond MRI to other imaging modalities, including: Positron Emission Tomography (PET) (Sweet and Brownell, 1953; Ter-Pogossian et al., 1975); Computed Tomography (CT) (Oldendorf, 1978); Single-Photon Emission Computed Tomography (SPECT) (Bruyant, 2002; Elhendy et al., 2002); Diffuse Optical Imaging/Tomography (DOI/DOT) (Martelli et al., 2009; Durduran et al., 2010); Magnetoencephalography (MEG) (Cohen, 1968, 1972).

Future work will extend this analysis to larger datasets, incorporating functional MRI (fMRI) to explore how functional connectivity patterns evolve with age. We also aim to integrate higher-order statistics beyond the bispectrum, including the trispectrum, to capture even more nuanced structural changes. Another promising direction is longitudinal tracking of individuals to detect early markers of dementia.

Our brain age regression pipeline includes robust statistical methods for estimating uncertainties in brain age predictions. This enhances clinical applicability, making it a viable tool for medical diagnostics and research.

In analogy to cosmology, where the large-scale structure of the universe is characterized by a set of cosmological parameters, the brain might be described by a limited set of fundamental parameters that define an individual's characteristic neuroanatomical state. Identifying such parameters could provide new biomarkers for neurological health.

This research opens avenues for improved diagnosis and treatment of neurodegenerative conditions such as Alzheimer's, advancing our understanding of brain aging processes and providing valuable tools for clinicians and researchers alike.

Appendix A. Database

We use data from the `OASIS-3` database (LaMontagne et al., 2019). All MRI data was collected through the Knight Alzheimer Research Imaging Program at Washington University in St. Louis, MO, USA. Some of the MRI data was collected on a Siemens Vision 1.5T, while the majority of the scans came from two different versions of a Siemens TIM Trio 3T (Siemens Medical Solutions USA, Inc). Participants were lying in the scanner in a supine position, head motion was minimized by inserting foam pads between the participant's head and antenna coil, and for some participants a vitamin E

capsule was placed over the left temple to mark lateralisation. A 16 channel head coil was used in all scans. Although a variety of different structural and functional imaging protocols are included in the OASIS dataset such as FLAIR, DTI and ASL, here we focused on the T1w scans. The T1w images were acquired using a 3DMPRAGE protocol TI/TR/TE: 1000/2400/3.08 ms, flip angle = 8°, resulting in 1 mm isotropic voxels.

Data were provided by OASIS-3: Longitudinal Multimodal Neuroimaging: Principal Investigators: T. Benzinger, D. Marcus, J. Morris; NIH P30 AG066444, P50 AG00561, P30 NS09857781, P01 AG026276, P01 AG003991, R01 AG043434, UL1 TR000448, R01 EB009352. AV-45 doses were provided by Avid Radiopharmaceuticals, a wholly owned subsidiary of Eli Lilly.

Appendix A.1. Selection of `OASIS-3` sample

Starting from the `OASIS-3` database, we define a sample of "healthy" subjects, characterized as individuals who have not yet developed dementia (based on their Clinical Dementia Rating, CDR) and who do not suffer from any other active conditions in their clinical records. Based on this criterion, we select 401 unique participants, of whom 58% are women and 42% are men. For these "healthy" subjects, we analyze all available T1-weighted (T1w) MRI images in native space using a higher-order statistical pipeline. The dataset under study consists of 864 MRI sessions, covering a chronological age range from 42 to 98 years (see Figure A.6). We refer to this as the complete sample (CS).

Appendix A.2. Preprocessing of the calibration sample

We pre-process the T1-weighted (T1w) MRI data using the HCP minimal processing pipeline, as described by Glasser et al. (2013). This process standardizes all images to a resolution of 1 mm, including alignment and the removal of skull and non-brain tissues. In most cases, we follow the standard HCP configuration. However, when T2-weighted (T2w) or field-map images are unavailable, we adapt the pipeline using the available imaging data, without applying the HCP-specific method to achieve reference precision.

Cortical reconstruction and volumetric segmentation were performed with the convolutional neural network `FastSurfer` suite (Henschel et al., 2020, 2022; Faber et al., 2022; Estrada et al., 2023), which performs an equivalent analysis to the widely used `FreeSurfer` image analysis suite. The technical details of these procedures are described in prior publications (Dale et al., 1999; Fischl et al., 1999; Fischl and Dale, 2000; Fischl et al., 2001, 2002,

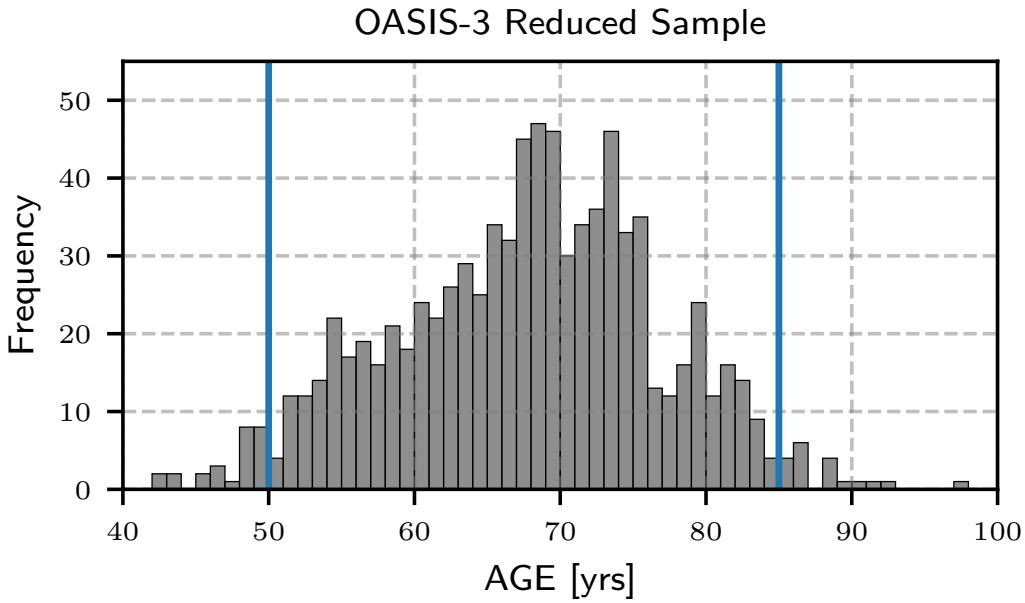

Figure A.6: Age distribution for the `OASIS-3` dataset used in the analysis. The vertical lines show the lower and upper limit to select the RS sample used in the validation.

2004b,a; Segonne et al., 2004; Han et al., 2006; Jovicich et al., 2006; Reuter et al., 2010, 2012).

Appendix B. Power-spectra and bispectra computations

We employ the FFTW algorithm to compute both the power-spectrum and bispectrum. The process begins by transforming the dataset, originally consisting of 3D voxels in NIfTI format (with a 1mm resolution), onto a cubical mesh with side length of 300 mm and 300^3 voxels, centered on the brain. We adapted a cosmological code (Zhao et al., 2021), traditionally used to estimate the bispectrum in cosmological simulations [in units of h^{-1} Mpc; 1 Mpc $= 3.086 \times 10^{22}$ m; $h = H_0/(100\text{km/s/Mpc})$ with H_0 being Hubble's constant], to work with MRI data (see also Kitaura et al., 2016). This involves a direct translation from millimeters to h^{-1} Mpc (1 mm $= 1\ h^{-1}$ Mpc in numerical code units), while operating directly on MRI intensity values instead of density fluctuations as in cosmological applications. Throughout the analysis, we use a Nearest-Grid-Point (NGP) assignment kernel.

Given the intricate structure of the brain and the associated complexity

across various scales, numerous configurations need to be sampled. To reduce the otherwise vast parameter space, we restrict the triangle sizes in Fourier-space to the range $0.1 < k < 2$ mm^{-1} corresponding to spanning spatial scales from ∼3 to 63 mm. The lower bound excludes large-scale effects that may be dominated by boundary issues, while the upper bound, set at twice the grid resolution (1mm), helps to prevent aliasing artifacts (see, e.g., Press et al., 1992; Jing, 2005).

Appendix C. Metrics used in this study

- **Bispectrum variance**: $\mathrm{Var}(x) = \frac{1}{l-1}\sum_{i=1}^{l}(x_i - \bar{x})^2$ with $\bar{x} = \frac{1}{l}\sum_{i=1}^{l} x_i$, where x_i is the bispectrum value for an angle θ at bin i and l being the total number of θ bins.

- **MAE (mean absolute error)**: $\frac{1}{n}\sum_{i=1}^{n}|y_i - \hat{y}_i|$ with y_i and $\hat{y}_i$ being the predicted and true age values for session i out of n sessions, respectively. The data array vector conformed by all predicted ages is given by Y, while for the true ages it is $\hat{Y}$.

- **Outlier**: $|\Delta\mathrm{AGE}_i| = |y_i - \hat{y}_i| > 7$ years.

- **Geometric Mean (G-Mean)** for the classification performance is calculated as the geometric mean of the sensitivities across all age groups:

  G-Mean $= (\prod_{i=1}^{m} S_i)^{\frac{1}{m}}$, where m is the total number of age groups or classes, and: $S_i = \frac{T_i^+}{T_i^+ + F_i^-}$

  is the sensitivity (recall) for class (age group) i, T^+ are the true positives and F^- are the false negatives. A true positive occurs when the model correctly predicts that a subject belongs to their true age group. A false negative occurs when a subject truly belongs to a specific age group, but the model predicts them to be outside that group.

- **Kendall's correlation coefficient** calculation steps:

  1. Rank the subjects:

     Rank all subjects based on their bispectrum values for the specific configuration we are analyzing. Separately, rank the same subjects by their biological ages.

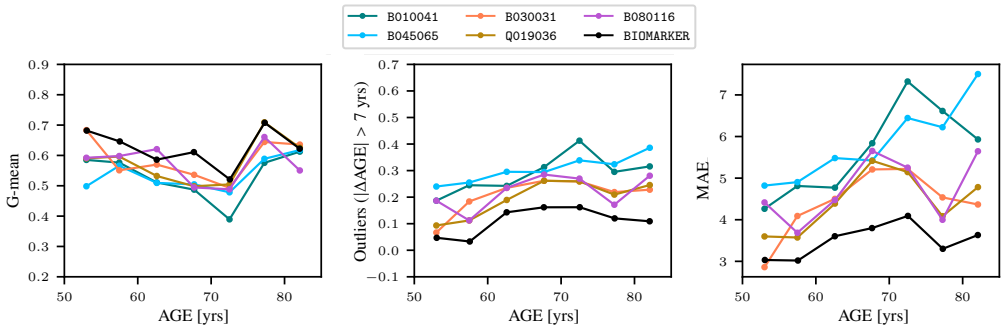

Figure C.7: Metric details of singular configurations and the proposed biomarker for the RS sample.

2. Compare pairs of subjects:

   For every pair of subjects, determine if the ranks of both variables (bispectrum and biological age) are consistent:

   – Concordant pair: If one subject has a higher bispectrum value and is also older, or if one has a lower bispectrum value and is also younger.

   – Discordant pair: If one subject has a higher bispectrum value but is younger, or has a lower bispectrum value but is older.

3. Compute $\tau = \frac{C-D}{\sqrt{(C+D+A)(X+D+B)}}$, with C and D being the number of concordant and discordant pairs, respectively; A the number of ties only in Y, and B the number of ties only in $\hat{Y}$.

The metrics corresponding to the singular bispectrum configurations and the combined one are shown as a function of age groups in Figure C.7.

Appendix D. Summary of the method

The following steps are outlined in Figure 2:

1. **MRI data preparation:** We start with the selection and preprocessing of MRI data and representation of intensity distribution on a cubical regular mesh (see Appendix A).

2. **Higher-order statistical three-dimensional spatial frequency analysis**

   (a) **Fourier-space calculations:** We Fourier transform each MRI data cube and compute its power-spectrum and bispectra for a large variety of configurations. The power-spectra are used to construct the hierarchical models, which in turn are used to compute the reduced bispectra (see bottom panel in Figure 2 and Appendix B).

   (b) **Pre-classification scale-dependent analysis of systematics:** We analyze the variance of the bispectra across different age groups. Outliers, likely due to dementia or MRI measurement issues, exhibit significant deviations from the average variance within their respective age group. To ensure the integrity of the dataset, we apply a conservative exclusion criterion. Initially, we focus on the raw and reduced bispectrum configurations with the smallest variance variations across age, in order to better address systematics. The configurations identified are ($k_1 = 0.13$, $k_2 = 0.57\ \mathrm{mm}^{-1}$) for the raw bispectrum and ($k_1 = 0.59$, $k_2 = 0.80\ \mathrm{mm}^{-1}$) for the reduced bispectrum.

   Next, we exclude sessions that deviate by more than $\gtrsim$3 standard deviations from the mean variance. As a result, we reduce the dataset from 921 sessions to 880 using the reduced bispectrum and to 864 using the raw bispectrum.

   We then further refine the sample based on the number density of sessions for individuals below and above the age thresholds shown in Figure A.6. This yields a subsample of 827 sessions, which we refer to as the reduced sample (RS).

   (c) **Classification and scale-dependent correlation analysis:** We analyze Kendall's rank correlation coefficients between configurations and age (see Figure D.8). Additionally, we apply a Random Forest classifier, computing the G-mean and MAE for each singular bispectrum configuration. The configurations with the highest G-means and lowest MAEs are identified and considered. These top-performing configurations are then combined in all possible ways to reduce the selection to a minimal set, capturing the most important characteristic scales.

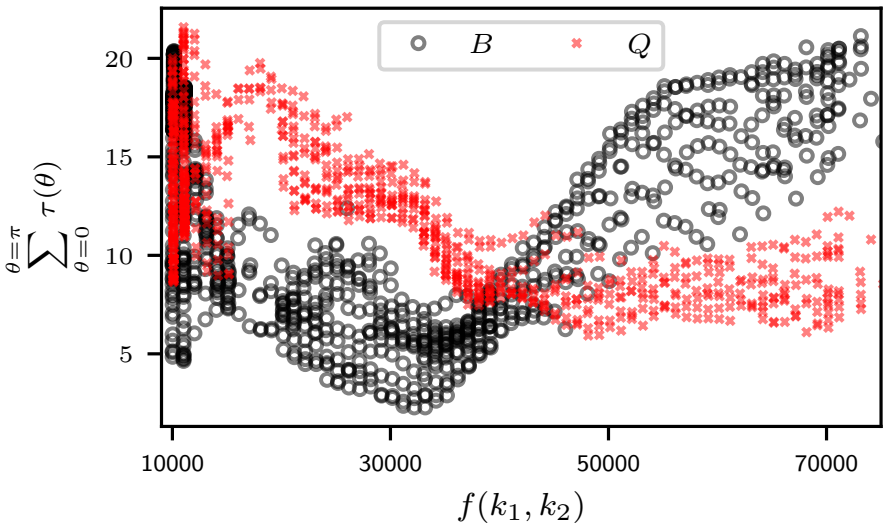

Figure D.8: Sum of Kendall's rank correlation coefficient between configurations and age for the CS sample. The x-axis represents a combination of $f(k_1, k_2) = 100000 \times k_1 + 100 \times k_2$, while the y-axis shows the sum of τ within θ-bins of $2^\circ\ 15'$ arcminutes. The trend at ~ 70000 continues to higher k-configurations. This representation highlights the dependence on k_1: $k_1 \sim f(k_1, k_2)/10^5$, e.g., $f(k_1, k_2) = 50000 : k_1 \sim 0.5$.

The Kendall coefficients support our choice of pre-classification analysis for systematics. According to $f(k_1, k_2)$, the raw bispectrum with the lowest correlation with age is $\lesssim 40000$ for $k_1 \lesssim 0.4$ mm^{-1}, while for the reduced bispectrum, it is $\gtrsim 50000$ for $k_1 \gtrsim 0.5$ mm^{-1}.

(d) **Post-classification analysis of systematics:**
Individual MRI data with large deviations from the true underlying age, based on the criterion $|\Delta\text{AGE}| > 7$ years, are classified as outliers. Currently, this criterion is not being applied to further filter the data sample; instead, it serves solely as a quality assessment measure for the biomarker.

(e) We develop an **age-regression neural network** integrating the selected bispectrum configurations into a multi-input architecture. Each configuration is processed through dense layers employing ReLU activations. The resulting features are concatenated and passed through fully connected layers with batch normalization, L2 regularization, and dropout to improve generalization. The

Table D.1: Summary of singular configurations making the `OASIS-3` biomarker

	k_1 (mm^{-1})	k_2 (mm^{-1})	r_1 (mm)	r_2 (mm)	θ (rad)	Name
B	0.10	0.41	62.83	15.32	0.5-2.5	`B010041`
Q	0.19	0.36	33.07	17.45	0.-3.15	`Q019036`
B	0.30	0.31	20.94	20.27	2.-3.15	`B030031`
B	0.45	0.65	13.96	9.67	0.4-1.5	`B045065`
B	0.80	1.16	7.85	5.43	0.-3.15	`B080116`

final output layer applies a softplus activation with a bias initializer to stabilize the predicted age values. The model is trained using mean absolute error (MAE) loss and optimized with Adam using an exponential learning rate decay schedule. This is the methodology employed to estimate ages shown in the right panel of Figure 2.

(f) Alternatively, we can apply **neural density estimators**, which compute the uncertainty for each individual subject as opposed to an average error estimation (see Figure 4 and section on the neural density estimators below).

The process outlined above can be extended to an iterative scheme, where consistency between the data and their metrics is pursued based on robust statistical criteria.

The five top singular bispectrum configurations conforming the biomarker as obtained with this method are summarised in Table D.1.

Appendix D.1. Neural Density Estimator

We use a normalizing flow (NF) based amortized inference approach (see Cranmer et al., 2020, and references therein) with the python ltu-ili package (`https://github.com/maho3/ltu-ili`).

The NF is trained to estimate the posterior distribution of the age given the higher-order summary statistics extracted from the bispectrum. Because of the high number of features, we use an embedding network which is simultaneously optimized. The embedding network is composed of a Recurrent Neural Network (RNN) followed by fully connected layers.

The RNN processes sequences with an input size of 268 features, uses 128 hidden units, and has 2 stacked layers. The output is then passed through fully connected layers for further transformation.

We use the sbi library's neural density posterior estimators (NPE with different configurations):

- MADE (Masked Autoencoder for Distribution Estimation): Configured with different numbers of hidden features (100, 50) and transformation layers (100).
- MDN (Mixture Density Network): Configured with 128 hidden features and 1 component.

The training data was randomly selected from the portion of the CS sample highlighted as the shaded region in Figure A.6. A total of 459 MRI sessions from the CS sample and 437 from the RS sample were used for training in the calculations shown in Figure 4.

Appendix E. Application to the `Cam-CAN` dataset

Once the final dataset and biomarker configurations are defined, we perform age regression. In particular, we apply the methodology outlined in Appendix D independently to the `Cam-CAN` dataset (Taylor et al., 2017; Liem et al., 2017).

Systematic differences between the `OASIS-3` and `Cam-CAN` databases, clearly illustrated by intensity distribution inconsistencies shown in Figure E.9, prevented us from applying the previously identified `OASIS-3` bispectrum configurations directly to the `Cam-CAN` dataset. Consequently, we conducted an analogous configuration selection study specifically for `Cam-CAN`. The five optimal configurations identified for `Cam-CAN` differ from those derived for OASIS-3, although they share certain characteristics: notably, these configurations generally feature very different side lengths ($k_2 \gg k_1$) and span from large to small scales, effectively capturing various physiological brain aging processes. Median values as a function of age, for `Cam-CAN` configurations are found in Figure E.10.

We processed the dataset with the same HCP Pipeline, resulting in 645 MRI sessions, spanning an age range from 18 to 88 years (shown in Figure E.11) with a much lower density of sessions per age. We repeated the

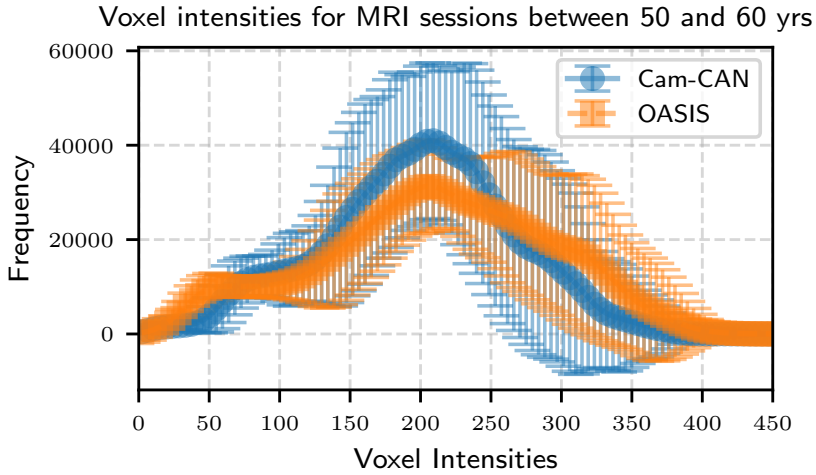

Figure E.9: Voxel intensity distributions and corresponding standard deviations for MRI sessions aged between 50 and 60 years from the `OASIS-3` and `Cam-CAN` datasets. The differences observed within this age range are consistent across all other age groups. Note that standard deviations do not account for the inherent positivity constraint on intensity values.

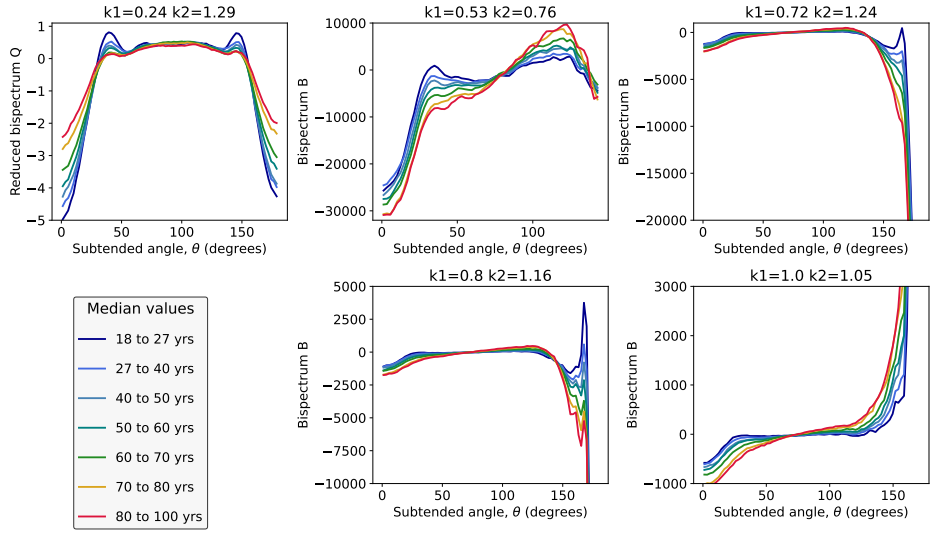

Figure E.10: Median bispectra per age group for the individual configurations that enter the biomarker definition from the `Cam-CAN` dataset. Here we consider the raw and reduced bispectra for fix $|\mathbf{k}_1|$ and $|\mathbf{k}_2|$ as a function of the subtended angle θ between both k-vectors: $B(\theta|k_1, k_2)$ and $Q(\theta|k_1, k_2)$.

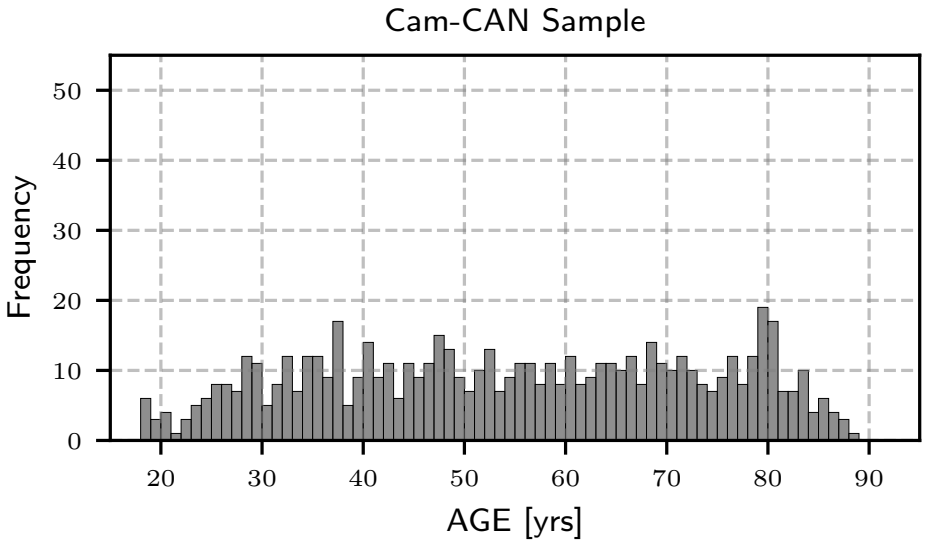

Figure E.11: Age distribution for the `Cam-CAN` dataset. The frequency axis is in the same scale as in Figure A.6, highlighting the density differences with respect to `OASIS-3` dataset.

Table E.2: Summary of singular configurations making the `Cam-CAN` biomarker

	k_1 (mm^{-1})	k_2 (mm^{-1})	r_1 (mm)	r_2 (mm)	θ (rad)	Name
Q	0.24	1.29	26.18	4.87	0.-3.15	`Q024129`
B	0.53	0.76	11.86	8.27	0.-2.5	`B053076`
B	0.72	1.24	8.73	5.07	0.-3.15	`B072124`
B	0.80	1.16	7.85	5.43	0.-3.15	`B080116`
B	1.0	1.05	6.28	5.98	0.-3.	`B010105`

search for the best configurations. Table E.2 lists the configurations selected for `Cam-CAN` and showed in Figure E.10.

Finally, we applied the age-regression neural network to the `Cam-CAN` dataset using leave-one-out validation to estimate ages for each session, achieving a mean absolute error (MAE) of approximately 3.4 years (see Figure E.12).

This result is consistent with the MAE of 3.6 years observed in the `OASIS-3` analysis. The similarity in performance suggests that these results might reflect an inherent limitation in precision achievable using higher-order

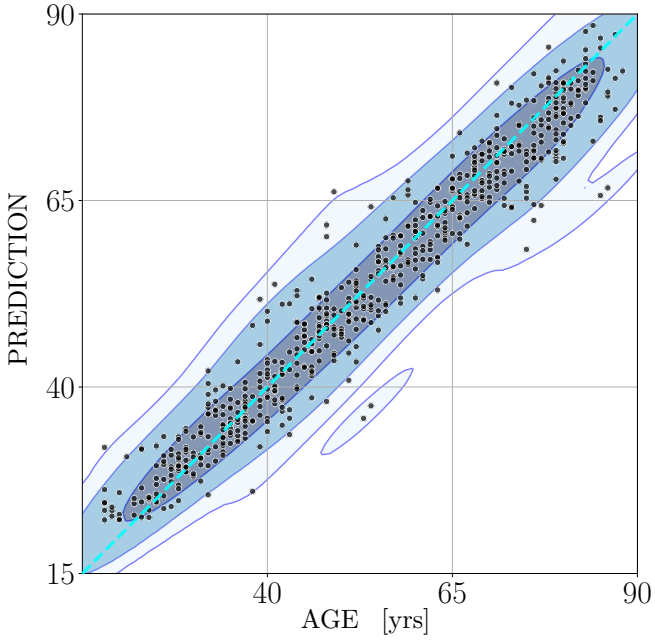

Figure E.12: Age regression for the `Cam-CAN` dataset. Using the leave-one-out technique, we estimate the age for all MRI sessions, resulting in a MAE of 3.4 years.

statistical methods, structural MRI with a specific resolution, or intrinsic uncertainty in brain age estimation due to the heterogeneity within human populations captured by these databases. The slightly broader age range of `Cam-CAN` might contribute to the observed marginal improvement, as the younger age populations show a smaller scatter.

Acknowledgements

The research conducted in this work was primarily funded by the Cabildo de Tenerife under IACTEC Technological Training Program, grant TF INNOVA, in support of the `Cosmic Brain` project starting in 2021 (PI: FSK). The authors acknowledge the Spanish Ministry of Economy and Competitiveness (MINECO) for financing the `Big Data of the Cosmic Web` project:

PID2020-120612GB-I00/AEI/10.13039/501100011033 (PI: FSK) and the *Cosmology with Large Scale Structure Probes* project funded by the IAC (PI: FSK), which provided numerical tools and computing facilities. NJ thanks financial support from PID2021-127611NB-I00 (PI: NJ).

Declaration of generative AI and AI-assisted technologies in the writing process

During the preparation of this work the author(s) used Writefull and ChatGPT to enhance the clarity and readability of the manuscript. After using this tool/service, the author(s) reviewed and edited the content as needed and take(s) full responsibility for the content of the publication.

References

Balian, R., Schaeffer, R., 1989. Scale-invariant matter distribution in the universe. Astronomy and Astrophysics 220, 1–29.

Bardeen, J.M., Bond, J.R., Kaiser, N., Szalay, A.S., 1986. The Statistics of Peaks of Gaussian Random Fields. Astrophysical Journal 304, 15. doi:10.1086/164143.

Baumgart, D.J., Fry, J.N., 1991. Fourier Spectra of Three-dimensional Data. Astrophysical Journal 375, 25. doi:10.1086/170166.

Bernardeau, F., Colombi, S., Gaztañaga, E., Scoccimarro, R., 2002. Large-scale structure of the Universe and cosmological perturbation theory. Physical Reports 367, 1–248. doi:10.1016/S0370-1573(02)00135-7, arXiv:astro-ph/0112551.

Bethlehem, R.A.I., Seidlitz, J., White, S.R., Vogel, J.W., Anderson, K.M., Adamson, C., Adler, S., Alexopoulos, G.S., Anagnostou, E., Areces-Gonzalez, A., Astle, D.E., Auyeung, B., Ayub, M., Bae, J., Ball, G., Baron-Cohen, S., Beare, R., Bedford, S.A., Benegal, V., Beyer, F., Blangero, J., Blesa Cábez, M., Boardman, J.P., Borzage, M., Bosch-Bayard, J.F., Bourke, N., Calhoun, V.D., Chakravarty, M.M., Chen, C., Chertavian, C., Chetelat, G., Chong, Y.S., Cole, J.H., Corvin, A., Costantino, M., Courchesne, E., Crivello, F., Cropley, V.L., Crosbie, J., Crossley, N., Delarue, M., Delorme, R., Desrivieres, S., Devenyi, G.A., Di Biase, M.A., Dolan, R., Donald, K.A., Donohoe, G., Dunlop, K., Edwards, A.D., Elison, J.T., Ellis, C.T., Elman, J.A., Eyler, L., Fair, D.A., Feczko, E., Fletcher, P.C., Fonagy, P., Franz, C.E., Galan-Garcia, L., Gholipour, A., Giedd, J., Gilmore, J.H., Glahn, D.C., Goodyer, I.M., Grant, P.E., Groenewold, N.A., Gunning, F.M., Gur, R.E., Gur, R.C., Hammill, C.F., Hansson, O., Hedden, T., Heinz, A., Henson, R.N., Heuer, K., Hoare, J., Holla, B.,

Holmes, A.J., Holt, R., Huang, H., Im, K., Ipser, J., Jack, C.R., Jackowski, A.P., Jia, T., Johnson, K.A., Jones, P.B., Jones, D.T., Kahn, R.S., Karlsson, H., Karlsson, L., Kawashima, R., Kelley, E.A., Kern, S., Kim, K.W., Kitzbichler, M.G., Kremen, W.S., Lalonde, F., Landeau, B., Lee, S., Lerch, J., Lewis, J.D., Li, J., Liao, W., Liston, C., Lombardo, M.V., Lv, J., Lynch, C., Mallard, T.T., Marcelis, M., Markello, R.D., Mathias, S.R., Mazoyer, B., McGuire, P., Meaney, M.J., Mechelli, A., Medic, N., Misic, B., Morgan, S.E., Mothersill, D., Nigg, J., Ong, M.Q.W., Ortinau, C., Ossenkoppele, R., Ouyang, M., Palaniyappan, L., Paly, L., Pan, P.M., Pantelis, C., Park, M.M., Paus, T., Pausova, Z., Paz-Linares, D., Pichet Binette, A., Pierce, K., Qian, X., Qiu, J., 3R-BRAIN, AIBL, Initiative, A.D.N., Investigators, A.D.R.W.B., Team, C.A.L.M., Cam-CAN, CCNP, COBRE, cVEDA, Group, E.D.B.A.W., Project, D.H.C., FinnBrain, Study, H.A.B., IMAGEN, KNE96, of Aging, T.M.C.S., NSPN, POND, Group, T.P.A.R., VETSA, 2022. Brain charts for the human lifespan. Nature 604, 525–533. URL: https://doi.org/10.1038/s41586-022-04554-y, doi:10.1038/s41586-022-04554-y.

Bhattarai, P., Thakuri, D.S., Nie, Y., Chand, G.B., 2024. Explainable ai-based deep-shap for mapping the multivariate relationships between regional neuroimaging biomarkers and cognition. European Journal of Radiology 174, 111403. URL: https://www.sciencedirect.com/science/article/pii/S0720048X24001190, doi:https://doi.org/10.1016/j.ejrad.2024.111403.

Breiman, L., 2001. Random forests. Machine Learning 45, 5–32. URL: https://doi.org/10.1023/A:1010933404324, doi:10.1023/A:1010933404324.

Bruyant, P.P., 2002. Analytic and iterative reconstruction algorithms in spect. Journal of Nuclear Medicine 43, 1343–1358.

Choi, J.D., Moon, Y., Kim, H.J., Yim, Y., Lee, S., Moon, W.J., 2022. Choroid plexus volume and permeability at brain MRI within the alzheimer disease clinical spectrum. Radiology 304, 635–645.

Cohen, D., 1968. Magnetoencephalography: evidence of magnetic fields produced by alpha-rhythm currents. Science 161, 784–786. doi:10.1126/science.161.3843.784.

Cohen, D., 1972. Magnetoencephalography: detection of the brain's electrical activity with a superconducting magnetometer. Science 175, 664–666. doi:10.1126/science.175.4022.664.

Cole, J.H., Poudel, R.P., Tsagkrasoulis, D., Caan, M.W., Steves, C., Spector, T.D., Montana, G., 2017. Predicting brain age with deep learning from raw imaging data results in a reliable and heritable biomarker. NeuroImage 163, 115–124. URL: https://www.sciencedirect.com/science/article/pii/S1053811917306407, doi:https://doi.org/10.1016/j.neuroimage.2017.07.059.

Cranmer, K., Brehmer, J., Louppe, G., 2020. The frontier of simulation-based inference. Proceedings of the National Academy of Science 117, 30055–30062. doi:10.1073/pnas.1912789117, arXiv:1911.01429.

Creminelli, P., Pitrou, C., Vernizzi, F., 2011. The CMB bispectrum in the squeezed limit. Journal of Cosmology and Astroparticle Physics 2011, 025. doi:10.1088/1475-7516/2011/11/025, arXiv:1109.1822.

Dale, A., Fischl, B., Sereno, M.I., 1999. Cortical surface-based analysis: I. segmentation and surface reconstruction. NeuroImage 9, 179 – 194.

Dani, N., Herbst, R.H., McCabe, C., Green, G.S., Kaiser, K., Head, J.P., Cui, J., Shipley, F.B., Jang, A., Dionne, D., Nguyen, L., Rodman, C., Riesenfeld, S.J., Prochazka, J., Prochazkova, M., Sedlacek, R., Zhang, F., Bryja, V., Rozenblatt-Rosen, O., Habib, N., Regev, A., Lehtinen, M.K., 2021. A cellular and spatial map of the choroid plexus across brain ventricles and ages. Cell 184, 3056–3074.e21.

Danielsen, V.M., Vidal-Piñeiro, D., Mowinckel, A.M., Sederevicius, D., Fjell, A.M., Walhovd, K.B., Westerhausen, R., 2020. Lifespan trajectories of relative corpus callosum thickness: Regional differences and cognitive relevance. Cortex 130, 127–141. URL: https://www.sciencedirect.com/science/article/pii/S0010945220302227, doi:https://doi.org/10.1016/j.cortex.2020.05.020.

Durduran, T., Choe, R., Baker, W.B., Yodh, A.G., 2010. Diffuse optics for tissue monitoring and tomography. Reports on Progress in Physics 73, 076701. doi:10.1088/0034-4885/73/7/076701.

Elhendy, A., Bax, J.J., Poldermans, D., 2002. Dobutamine stress myocardial perfusion imaging in coronary artery disease. Journal of Nuclear Medicine 43, 1634–1646.

Estrada, S., Kügler, D., Bahrami, E., Xu, P., Mousa, D., Breteler, M.M., Aziz, N.A., Reuter, M., 2023. Fastsurfer-hypvinn: Automated subsegmentation of the hypothalamus and adjacent structures on high-resolutional brain mri. Imaging Neuroscience 1, 1–32. URL: https://doi.org/10.1162/imag_a_00034, doi:10.1162/imag_a_00034.

Faber, J., Kügler, D., Bahrami, E., Heinz, L.S., Timmann, D., Ernst, T.M., Deike-Hofmann, K., Klockgether, T., van de Warrenburg, B., van Gaalen, J., Reetz, K., Romanzetti, S., Oz, G., Joers, J.M., Diedrichsen, J., Giunti, P., Garcia-Moreno, H., Jacobi, H., Jende, J., de Vries, J., Povazan, M., Barker, P.B., Steiner, K.M., Krahe, J., Reuter, M., 2022. Cerebnet: A fast and reliable deep-learning pipeline for detailed cerebellum sub-segmentation. NeuroImage 264, 119703. URL: https://www.sciencedirect.com/science/article/pii/S1053811922008242, doi:https://doi.org/10.1016/j.neuroimage.2022.119703.

Fisch, L., Leenings, R., Winter, N.R., Dannlowski, U., Gaser, C., Cole, J.H., Hahn, T., 2021. Editorial: Predicting chronological age from structural neuroimaging: The predictive analytics competition 2019. Front Psychiatry 12, 710932.

Fischl, B., Dale, A.M., 2000. Measuring the thickness of the human cerebral cortex from magnetic resonance images. Proceedings of the National Academy of Sciences of the United States of America 97, 11050–11055. arXiv:http://www.pnas.org/content/97/20/11050.full.pdf+html.

Fischl, B., Liu, A., Dale, A.M., 2001. Automated manifold surgery: constructing geometrically accurate and topologically correct models of the human cerebral cortex. IEEE Medical Imaging 20, 70–80.

Fischl, B., Salat, D.H., Busa, E., Albert, M., Dieterich, M., Haselgrove, C., van der Kouwe, A., Killiany, R., Kennedy, D., Klaveness, S., Montillo, A., Makris, N., Rosen, B., Dale, A.M., 2002. Whole brain segmentation: automated labeling of neuroanatomical structures in the human brain. Neuron 33, 341–355.

Fischl, B., Salat, D.H., van der Kouwe, A.J.W., Makris, N., Ségonne, F., Quinn, B.T., Dale, A.M., 2004a. Sequence-independent segmentation of magnetic resonance images. NeuroImage 23, S69 – S84. URL: http://www.sciencedirect.com/science/article/B6WNP-4DCMGVT-2/2/7eee26326dc63f931b826eac33becc8b, doi:DOI:10.1016/j.neuroimage.2004.07.016. mathematics in Brain Imaging.

Fischl, B., Sereno, M.I., Dale, A., 1999. Cortical surface-based analysis: Ii: Inflation, flattening, and a surface-based coordinate system. NeuroImage 9, 195 – 207.

Fischl, B., van der Kouwe, A., Destrieux, C., Halgren, E., Ségonne, F., Salat, D.H., Busa, E., Seidman, L.J., Goldstein, J., Kennedy, D., Caviness, V., Makris, N., Rosen, B., Dale, A.M., 2004b. Automatically Parcellating the Human Cerebral Cortex. Cerebral Cortex 14, 11–22. URL: http://cercor.oxfordjournals.org/content/14/1/11.abstract, doi:10.1093/cercor/bhg087.

Frieman, J.A., Gaztanaga, E., 1994. The Three-Point Function as a Probe of Models for Large-Scale Structure. Astrophysical Journal 425, 392. doi:10.1086/173995, arXiv:astro-ph/9306018.

Fry, J.N., 1984a. Galaxy N-point correlation functions - Theoretical amplitudes for arbitrary N. Astrophysical Journal Letters 277, L5–L8. doi:10.1086/184189.

Fry, J.N., 1984b. The Galaxy correlation hierarchy in perturbation theory. Astrophysical Journal 279, 499–510. doi:10.1086/161913.

Fry, J.N., Peebles, P.J.E., 1978. Statistical analysis of catalogs of extragalactic objects. IX. The four-point galaxy correlation function. Astrophysical Journal 221, 19–33. doi:10.1086/156001.

Fujita, S., Mori, S., Onda, K., Hanaoka, S., Nomura, Y., Nakao, T., Yoshikawa, T., Takao, H., Hayashi, N., Abe, O., 2023. Characterization of Brain Volume Changes in Aging Individuals With Normal Cognition Using Serial Magnetic Resonance Imaging. JAMA Network Open 6, e2318153–e2318153. doi:10.1001/jamanetworkopen.2023.18153.

García-Farieta, J.E., Hortúa, H.J., Kitaura, F.S., 2024. Bayesian deep learning for cosmic volumes with modified gravity. Astronomy and Astrophysics 684, A100. doi:10.1051/0004-6361/202347929, arXiv:2309.00612.

Glasser, M.F., Sotiropoulos, S.N., Wilson, J.A., Coalson, T.S., Fischl, B., Andersson, J.L., Xu, J., Jbabdi, S., Webster, M., Polimeni, J.R., Van Essen, D.C., Jenkinson, M., 2013. The minimal preprocessing pipelines for the human connectome project. NeuroImage 80, 105–124. URL: https://www.sciencedirect.com/science/article/pii/S1053811913005053, doi:https://doi.org/10.1016/j.neuroimage.2013.04.127. mapping the Connectome.

Groth, E.J., Peebles, P.J.E., 1977. Statistical analysis of catalogs of extragalactic objects. VII. Two- and three-point correlation functions for the high-resolution Shane-Wirtanen catalog of galaxies. Astrophysical Journal 217, 385–405. doi:10.1086/155588.

Han, X., Jovicich, J., Salat, D., van der Kouwe, A., Quinn, B., Czanner, S., Busa, E., Pacheco, J., Albert, M., Killiany, R., Maguire, P., Rosas, D., Makris, N., Dale, A., Dickerson, B., Fischl, B., 2006. Reliability of MRI-derived measurements of human cerebral cortical thickness: The effects of field strength, scanner upgrade and manufacturer. NeuroImage 32, 180–194.

Hastie, T., Tibshirani, R., Friedman, J., 2001. The Elements of Statistical Learning: Data Mining, Inference, and Prediction. Springer series in statistics, Springer.

Hausdorff, F., 1921a. Summationsmethoden und momentfolgen. i. Mathematische Zeitschrift 9, 74–109.

Hausdorff, F., 1921b. Summationsmethoden und momentfolgen. ii. Mathematische Zeitschrift 9, 280–299. URL: https://doi.org/10.1007/BF01279032, doi:10.1007/BF01279032.

Henschel, L., Conjeti, S., Estrada, S., Diers, K., Fischl, B., Reuter, M., 2020. Fastsurfer - a fast and accurate deep learning based neuroimaging pipeline. NeuroImage 219, 117012. URL: https://www.sciencedirect.com/science/article/pii/S1053811920304985, doi:https://doi.org/10.1016/j.neuroimage.2020.117012.

Henschel, L., Kügler, D., Reuter, M., 2022. Fastsurfervinn: Building resolution-independence into deep learning segmentation methods—a solution for highres brain mri. NeuroImage 251, 118933. URL: https://www.sciencedirect.com/science/article/pii/S1053811922000623, doi:https://doi.org/10.1016/j.neuroimage.2022.118933.

Hindriks, R., Broeders, T.A.A., Schoonheim, M.M., Douw, L., Santos, F., van Wieringen, W., Tewarie, P.K.B., 2024. Higher-order functional connectivity analysis of resting-state functional magnetic resonance imaging data using multivariate cumulants. Human Brain Mapping 45, e26663. URL: https://doi.org/10.1002/hbm.26663, doi:10.1002/hbm.26663. published by Wiley Periodicals LLC.

Jing, Y.P., 2005. Correcting for the Alias Effect When Measuring the Power Spectrum Using a Fast Fourier Transform. Astrophysical Journal 620, 559–563. doi:10.1086/427087, arXiv:astro-ph/0409240.

Jovicich, J., Czanner, S., Greve, D., Haley, E., van der Kouwe, A., Gollub, R., Kennedy, D., Schmitt, F., Brown, G., MacFall, J., Fischl, B., Dale, A., 2006. Reliability in multi-site structural mri studies: Effects of gradient non-linearity correction on phantom and human data. NeuroImage 30, 436 – 443. URL: http://www.sciencedirect.com/science/article/B6WNP-4HM7S0B-2/2/4fa5ff26cad90ba3c9ed12b7e12ce3b6, doi:DOI:10.1016/j.neuroimage.2005.09.046.

Kendall, M.G., 1938. A new measure of rank correlation. Biometrika 30, 81–89. doi:10.1093/biomet/30.1-2.81.

Kendall, M.G., 1945. The treatment of ties in ranking problems. Biometrika 33, 239–251.

Khintchine, A., 1934. Korrelationstheorie der stationären stochastischen prozesse. Mathematische Annalen 109, 604–615. doi:10.1007/BF01449156.

Kitaura, F.S., 2012. Non-Gaussian gravitational clustering field statistics. Monthly Notices of the Royal Astronomical Society 420, 2737–2755. doi:10.1111/j.1365-2966.2011.19680.x, arXiv:1012.3168.

Kitaura, F.S., Gil-Marín, H., Scóccola, C.G., Chuang, C.H., Müller, V., Yepes, G., Prada, F., 2015. Constraining the halo bispectrum in real

and redshift space from perturbation theory and non-linear stochastic bias. Monthly Notices of the Royal Astronomical Society 450, 1836–1845. doi:10.1093/mnras/stv645, arXiv:1407.1236.

Kitaura, F.S., Rodríguez-Torres, S., Chuang, C.H., Zhao, C., Prada, F., Gil-Marín, H., Guo, H., Yepes, G., Klypin, A., Scóccola, C.G., Tinker, J., McBride, C., Reid, B., Sánchez, A.G., Salazar-Albornoz, S., Grieb, J.N., Vargas-Magana, M., Cuesta, A.J., Neyrinck, M., Beutler, F., Comparat, J., Percival, W.J., Ross, A., 2016. The clustering of galaxies in the SDSS-III Baryon Oscillation Spectroscopic Survey: mock galaxy catalogues for the BOSS Final Data Release. Monthly Notices of the Royal Astronomical Society 456, 4156–4173. doi:10.1093/mnras/stv2826, arXiv:1509.06400.

Kumari, L.K.S., Sundarrajan, R., 2024. A review on brain age prediction models. Brain Research 1823, 148668. doi:10.1016/j.brainres.2023.148668. epub 2023 Nov 10. Declaration of Competing Interest: The authors declare that they have no known competing financial interests or personal relationships that could have appeared to influence the work reported in this paper.

LaMontagne, P.J., Benzinger, T.L.S., Morris, J.C., Keefe, S., Hornbeck, R., Xiong, C., Grant, E., Hassenstab, J., Moulder, K., Vlassenko, A.G., Raichle, M.E., Cruchaga, C., Marcus, D., 2019. Oasis-3: Longitudinal neuroimaging, clinical, and cognitive dataset for normal aging and alzheimer disease. medRxiv URL: https://www.medrxiv.org/content/early/2019/12/15/2019.12.13.19014902, doi:10.1101/2019.12.13.19014902.

Liem, F., Varoquaux, G., Kynast, J., Beyer, F., Kharabian Masouleh, S., Huntenburg, J.M., Lampe, L., Rahim, M., Abraham, A., Craddock, R.C., Riedel-Heller, S., Luck, T., Loeffler, M., Schroeter, M.L., Witte, A.V., Villringer, A., Margulies, D.S., 2017. Predicting brain-age from multimodal imaging data captures cognitive impairment. NeuroImage 148, 179–188. URL: https://www.sciencedirect.com/science/article/pii/S1053811916306103, doi:https://doi.org/10.1016/j.neuroimage.2016.11.005.

Martelli, F., Del Bianco, S., Ismaelli, A., Zaccanti, G., 2009. Light Propagation through Biological Tissue and Other Diffusive Media: Theory, Solutions, and Software. doi:10.1117/3.824746.

Matarrese, S., Verde, L., Heavens, A.F., 1997. Large-scale bias in the Universe: bispectrum method. Monthly Notices of the Royal Astronomical Society 290, 651–662. doi:10.1093/mnras/290.4.651, arXiv:astro-ph/9706059.

Meng, D., Zhang, S., Huang, Y., Mao, K., Han, J.D.J., 2024. Application of ai in biological age prediction. Current Opinion in Structural Biology 85, 102777. URL: https://www.sciencedirect.com/science/article/pii/S0959440X24000046, doi:https://doi.org/10.1016/j.sbi.2024.102777.

More, S., Antonopoulos, G., Hoffstaedter, F., Caspers, J., Eickhoff, S.B., Patil, K.R., 2023. Brain-age prediction: A systematic comparison of machine learning workflows. NeuroImage 270, 119947. URL: https://www.sciencedirect.com/science/article/pii/S1053811923000940, doi:https://doi.org/10.1016/j.neuroimage.2023.119947.

Oldendorf, W.H., 1978. The quest for an image of brain: a brief historical and technical review of brain imaging techniques. Neurology 28, 517–533. doi:10.1212/wnl.28.6.517.

Oschwald, J., Guye, S., Liem, F., Rast, P., Willis, S., Röcke, C., Jäncke, L., Martin, M., Mérillat, S., 2019. Brain structure and cognitive ability in healthy aging: a review on longitudinal correlated change. Reviews in the Neurosciences 31, 1–57.

Pajer, E., Schmidt, F., Zaldarriaga, M., 2013. The Observed squeezed limit of cosmological three-point functions. Physical Review D 88, 083502. doi:10.1103/PhysRevD.88.083502, arXiv:1305.0824.

Peebles, P.J.E., 1980. The large-scale structure of the universe.

Pemantle, R., Wilson, M.C., Melczer, S., 2024. Analytic Combinatorics in Several Variables. Cambridge Studies in Advanced Mathematics. 2nd ed., Cambridge University Press.

Press, W.H., Teukolsky, S.A., Vetterling, W.T., Flannery, B.P., 1992. Numerical Recipes in C. Second ed., Cambridge University Press, Cambridge, USA.

Reuter, M., Rosas, H.D., Fischl, B., 2010. Highly accurate inverse consistent registration: A robust approach. NeuroImage 53, 1181–1196. doi:10.1016/j.neuroimage.2010.07.020.

Reuter, M., Schmansky, N.J., Rosas, H.D., Fischl, B., 2012. Within-subject template estimation for unbiased longitudinal image analysis. NeuroImage 61, 1402–1418. URL: http://dx.doi.org/10.1016/j.neuroimage.2012.02.084, doi:10.1016/j.neuroimage.2012.02.084.

Segonne, F., Dale, A.M., Busa, E., Glessner, M., Salat, D., Hahn, H.K., Fischl, B., 2004. A hybrid approach to the skull stripping problem in mri. NeuroImage 22, 1060 – 1075. URL: http://www.sciencedirect.com/science/article/B6WNP-4CF5CNY-1/2/33cc73136f06f019b2c11023e7a95341, doi:DOI:10.1016/j.neuroimage.2004.03.032.

Shafto, M.A., Tyler, L.K., Dixon, M., Taylor, J.R., Rowe, J.B., Cusack, R., Calder, A.J., Marslen-Wilson, W.D., Duncan, J., Dalgleish, T., Henson, R.N., Brayne, C., Matthews, F.E., Cam-CAN, 2014. The cambridge centre for ageing and neuroscience (cam-can) study protocol: a cross-sectional, lifespan, multidisciplinary examination of healthy cognitive ageing. BMC Neurology 14, 204. URL: https://doi.org/10.1186/s12883-014-0204-1, doi:10.1186/s12883-014-0204-1.

Shohat, J.A., Tamarkin, J.D., 1943. The problem of moments. 1, American Mathematical Soc.

Springel, V., White, S.D.M., Jenkins, A., Frenk, C.S., Yoshida, N., Gao, L., Navarro, J., Thacker, R., Croton, D., Helly, J., Peacock, J.A., Cole, S., Thomas, P., Couchman, H., Evrard, A., Colberg, J., Pearce, F., 2005. Simulations of the formation, evolution and clustering of galaxies and quasars. Nature 435, 629–636. doi:10.1038/nature03597, arXiv:astro-ph/0504097.

Stoyanov, J.M., Lin, G.D., Kopanov, P., 2020. New checkable conditions for moment determinacy of probability distributions. Theory of Probability & Its Applications 65, 497–509. URL: https://doi.org/10.1137/S0040585X97T990083, doi:10.1137/S0040585X97T990083.

Sweet, W.H., Brownell, G.L., 1953. Localization of brain tumors with positron emitters. Nucleonics 11, 40–45.

Taylor, J.R., Williams, N., Cusack, R., Auer, T., Shafto, M.A., Dixon, M., Tyler, L.K., Cam-CAN, Henson, R.N., 2017. The cambridge centre for ageing and neuroscience (cam-can) data repository: Structural and functional mri, meg, and cognitive data from a cross-sectional adult lifespan sample. NeuroImage 144, 262–269. URL: https://www.sciencedirect.com/science/article/pii/S1053811915008150, doi:https://doi.org/10.1016/j.neuroimage.2015.09.018. data Sharing Part II.

Ter-Pogossian, M.M., Phelps, M.E., Hoffman, E.J., Mullani, N.A., 1975. A positron-emission transaxial tomograph for nuclear imaging (PETT). Radiology 114, 89–98.

Vazza, F., Feletti, A., 2020. The quantitative comparison between the neuronal network and the cosmic web. Frontiers in Physics 8. URL: https://www.frontiersin.org/journals/physics/articles/10.3389/fphy.2020.525731, doi:10.3389/fphy.2020.525731.

Wen, J., Varol, E., Sotiras, A., Yang, Z., Chand, G.B., Erus, G., Shou, H., Abdulkadir, A., Hwang, G., Dwyer, D.B., Pigoni, A., Dazzan, P., Kahn, R.S., Schnack, H.G., Zanetti, M.V., Meisenzahl, E., Busatto, G.F., Crespo-Facorro, B., Romero-Garcia, R., Pantelis, C., Wood, S.J., Zhuo, C., Shinohara, R.T., Fan, Y., Gur, R.C., Gur, R.E., Satterthwaite, T.D., Koutsouleris, N., Wolf, D.H., Davatzikos, C., 2022. Multi-scale semi-supervised clustering of brain images: Deriving disease subtypes. Medical Image Analysis 75, 102304. URL: https://doi.org/10.1016/j.media.2021.102304, doi:10.1016/j.media.2021.102304. pMID: 34818611.

Wiener, N., 1930. Generalized harmonic analysis. Acta Mathematica 55, 117–258. doi:10.1007/bf02546511.

Yang, Z., Wen, J., Davatzikos, C., 2022. Surreal-GAN:Semi-Supervised Representation Learning via GAN for uncovering heterogeneous disease-related imaging patterns. arXiv e-prints , arXiv:2205.04523doi:10.48550/arXiv.2205.04523, arXiv:2205.04523.

Yang, Z., Wen, J., Erus, G., Govindarajan, S.T., Melhem, R., Mamourian, E., Cui, Y., Srinivasan, D., Abdulkadir, A., Parmpi, P., et al., 2024. Brain aging patterns in a large and diverse cohort of 49,482 individuals. Nature Medicine , 1–12.

Yin, C., Imms, P., Cheng, M., Amgalan, A., Chowdhury, N.F., Massett, R.J., Chaudhari, N.N., Chen, X., Thompson, P.M., Bogdan, P., Irimia, A., the Alzheimer's Disease Neuroimaging Initiative, Weiner, M.W., Aisen, P., Petersen, R., Jack, C.R.J., Jagust, W., Trojanowki, J.Q., Toga, A.W., Beckett, L., Green, R.C., Saykin, A.J., Morris, J.C., Perrin, R.J., Shaw, L.M., Khachaturian, Z., Carrillo, M., Potter, W., Barnes, L., Bernard, M., González, H., Ho, C., Hsiao, J.K., Jackson, J., Masliah, E., Masterman, D., Okonkwo, O., Ryan, L., Silverberg, N., Fleisher, A., Rafii, M., Raman, R., Jimenez, G., Donohue, M., Gessert, D., Salazar, J., Zimmerman, C., Walter, S., Miller, G., Coker, G., Clanton, T., Hergesheimer, L., Smith, S., Adegoke, O., Mahboubi, P., Moore, S., Pizzola, J., Shaffer, E., Sloan, B., Harvey, D., Bernstein, M., Borowski, B., Senjem, M., Ward, C., Landau, S., Koeppe, R.A., Reiman, E.M., Chen, K., Morris, J.C., Toga, A.W., Foroud, T.M., Rosen, H., Nelson, C., Zmuda, M., Butters, M., Lopez, O.L., Oakley, M., Simpson, D.M., 2023. Anatomically interpretable deep learning of brain age captures domain-specific cognitive impairment. Proceedings of the National Academy of Sciences 120, e2214634120. URL: https://www.pnas.org/doi/abs/10.1073/pnas.2214634120, doi:10.1073/pnas.2214634120.

Zhao, C., Chuang, C.H., Bautista, J., de Mattia, A., Raichoor, A., Ross, A.J., Hou, J., Neveux, R., Tao, C., Burtin, E., Dawson, K.S., de la Torre, S., Gil-Marín, H., Kneib, J.P., Percival, W.J., Rossi, G., Tamone, A., Tinker, J.L., Zhao, G.B., Alam, S., Mueller, E.M., 2021. The completed SDSS-IV extended Baryon Oscillation Spectroscopic Survey: 1000 multi-tracer mock catalogues with redshift evolution and systematics for galaxies and quasars of the final data release. Monthly Notices of the Royal Astronomical Society 503, 1149–1173. URL: https://doi.org/10.1093/mnras/stab510, doi:10.1093/mnras/stab510.